Available online at www.sciencedirect.com

SciVerse ScienceDirect

Advances in Space Research 51 (2013) 554–574

ADVANCES IN SPACE RESEARCH (a COSPAR publication)

www.elsevier.com/locate/asr

Empirical STORM-E model: I. Theoretical and observational basis

Christopher J. Mertens [a,*], Xiaojing Xu [b,1], Dieter Bilitza [c,2], Martin G. Mlynczak [d,3], James M. Russell III [e,4]

[a] NASA Langley Research Center, Science Directorate, Mail Stop 401B, Hampton, VA 23681-2199, USA
[b] Science Systems & Applications Inc., One Enterprise Parkway, Suite 200, Hampton, VA 2366, USA
[c] School of Physics, Astronomy, and Computational Sciences, George Mason University, 4400 University Drive, MS 3F3, Fairfax, VA 22030-4444, USA
[d] NASA Langley Research Center, Science Directorate, Mail Stop 457, Hampton, VA 23681-2199, USA
[e] Center for Atmospheric Sciences, Hampton University, Hampton, VA 23688, USA

Available online 19 September 2012

Abstract

Auroral nighttime infrared emission observed by the Sounding of the Atmosphere using Broadband Emission Radiometry (SABER) instrument onboard the Thermosphere–Ionosphere–Mesosphere Energetics and Dynamics (TIMED) satellite is used to develop an empirical model of geomagnetic storm enhancements to E-region peak electron densities. The empirical model is called STORM-E and will be incorporated into the 2012 release of the International Reference Ionosphere (IRI). The proxy for characterizing the E-region response to geomagnetic forcing is $NO^+(v)$ volume emission rates (VER) derived from the TIMED/SABER 4.3 μm channel limb radiance measurements. The storm-time response of the $NO^+(v)$ 4.3 μm VER is sensitive to auroral particle precipitation. A statistical database of storm-time to climatological quiet-time ratios of SABER-observed $NO^+(v)$ 4.3 μm VER are fit to widely available geomagnetic indices using the theoretical framework of linear impulse-response theory. The STORM-E model provides a dynamic storm-time correction factor to adjust a known quiescent E-region electron density peak concentration for geomagnetic enhancements due to auroral particle precipitation. Part II of this series describes the explicit development of the empirical storm-time correction factor for E-region peak electron densities, and shows comparisons of E-region electron densities between STORM-E predictions and incoherent scatter radar measurements. In this paper, Part I of the series, the efficacy of using SABER-derived $NO^+(v)$ VER as a proxy for the E-region response to solar-geomagnetic disturbances is presented. Furthermore, a detailed description of the algorithms and methodologies used to derive $NO^+(v)$ VER from SABER 4.3 μm limb emission measurements is given. Finally, an assessment of key uncertainties in retrieving $NO^+(v)$ VER is presented.
Published by Elsevier Ltd. on behalf of COSPAR.

Keywords: Auroral particle precipitation; Ionosphere; E-region; Magnetic storm; Infrared remote sensing; SABER

1. Introduction

STORM-E is an empirical model for adjusting a known quiescent ionospheric E-region electron density for geomagnetic activity (Mertens et al., 2007a,b, 2009b). The STORM-E model primarily accounts for enhancement in the E-region peak electron density due to particle precipitation and is best suited for application in the auroral oval region. The proxy used to derive an empirical storm-time correction to E-region electron densities is $NO^+(v)$ volume emission rates (VER), which are derived from 4.3 μm limb radiation measurements observed from the Sounding of the

* Corresponding author. Tel.: +1 757 864 2179; fax: +1 757 864 6326.
E-mail addresses: Christopher.J.Mertens@nasa.gov (C.J. Mertens), xiaojing.xu@ssaihq.com (X. Xu), dbilitza@gmu.edu (D. Bilitza), Martin.G.Mlynczak@nasa.gov (M.G. Mlynczak), James.Russell@hamptonu.edu (J.M. Russell III).
[1] Tel.: +1 757 951 1697; fax: +1 757 951 1900.
[2] Tel.: +1 301 286 1617; fax: +1 703 993 9300.
[3] Tel.: +1 757 864 5695; fax: +1 757 864 5695.
[4] Tel.: +1 757 728 6893; fax: +1 757 727 5090.

0273-1177/$36.00 Published by Elsevier Ltd. on behalf of COSPAR.
http://dx.doi.org/10.1016/j.asr.2012.09.009

Atmosphere using Broadband Emission Radiometry (SABER) instrument onboard the Thermosphere–Ionosphere–Mesosphere Energetics and Dynamics (TIMED) satellite (Russell et al., 1999). SABER-derived $NO^+(v)$ VER is the fundamental observation-based quantity used in STORM-E. The theoretical formulation used to develop the empirical STORM-E model, given the $NO^+(v)$ VER as input data, is presented in Part II of this series (Mertens et al., submitted for publication). In this paper, Part I of the series, the theoretical and numerical techniques used to retrieve $NO^+(v)$ VER from the SABER 4.3 μm limb emission measurements are described in detail.

A specific application of STORM-E is to provide a storm-time correction to the International Reference Ionosphere (IRI) E-region peak electron densities. Integration of STORM-E into IRI-2012 is currently underway. The IRI is a widely used data-based model for specification of ionospheric parameters and is recommended for international use by the Committee on Space Research (COSPAR) and the International Union of Radio Science (URSI) (Bilitza and Reinisch, 2008). An important capability of the IRI required for space-weather-related applications is the accurate characterization of ionospheric parameters during solar-geomagnetic storms. The goal of developing algorithms for updating IRI parameters during storm-time conditions remains a high priority of the IRI team. However, the specification of the ionospheric response to geomagnetic activity in IRI has been mainly focused on the F-region. The first attempt to incorporate geomagnetic influences into IRI was by Fuller-Rowell et al. (2000) and Araujo-Pradere et al. (2002, 2003, 2004) in the development of the STORM model. The STORM model provides a storm-time correction to F-region electron density peak concentrations, and demonstrates that the underlying ionospheric F-region response to solar-geomagnetic activity can be captured in a relatively simple empirical model. The success of the STORM model in accounting for geomagnetic variations in F-region electron densities prompted the adoption of a similar technique in the development of STORM-E.

The measurement data source used in the development of STORM-E is SABER 4.3 μm broadband limb radiance measurements. SABER has obtained continuous, global measurements since the launch of the TIMED satellite in December, 2001. Observations from the geomagnetic storms of solar cycle 23 have shown that nighttime SABER 4.3 μm limb radiance measurements can be enhanced by several orders of magnitude above the nominal $CO_2(v_3)$ contribution. Analysis of these measurements revealed that nighttime 4.3 μm radiance is dominated by $NO^+(v)$ vibration–rotation band emission during geomagnetically disturbed conditions (Mertens et al., 2009a,b, 2008, 2007a,b). During magnetic storms, auroral particle precipitation ionizes the neutral atmosphere, producing vibrationally excited NO^+ (i.e., $NO^+(v)$) through fast exothermic ion-neutral chemical reactions, which promptly emit in the 4.3 μm region (Mertens et al., 2007a, 2008). Since NO^+ is the terminal E-region ion, and by charge neutrality, the above discoveries suggest that $NO^+(v)$ 4.3 μm emission can provide an excellent proxy for characterizing the response of the E-region electron density to solar-geomagnetic disturbances. This conjecture is foundational to the development of STORM-E, and its validity is addressed throughout this two-part series of papers.

The remainder of the paper is organized as follows. Section 2 provides observational support for the plausibility of using $NO^+(v)$ 4.3 μm emission as a proxy for characterizing the E-region response to geomagnetic forcing. Explicitly, vertical profiles of $NO^+(v)$ VER are used as the E-region proxy. Section 2 also presents the method of deriving $NO^+(v)$ VER from SABER 4.3 μm limb radiance measurements. Results from the $NO^+(v)$ VER retrieval algorithm and an uncertainty assessment are given in Section 3. The summary and conclusions are presented in Section 4.

2. SABER-derived E-region proxy

The measurement quantity used to develop the empirical STORM-E model is SABER-derived nighttime $NO^+(v)$ 4.3 μm VER. During the daytime, radiative emission at 4.3 μm in the mesosphere, lower thermosphere and ionosphere (MLTI) is dominated by CO_2 due to solar pumping of the $CO_2(v_1, v_2, v_3)$ vibration–rotation bands (Lopez-Puertas et al., 1986a,b, 1998; Sharma and Wintersteiner, 1985; Nebel et al., 1994). Thus, any daytime auroral emission is a comparatively small enhancement above the nominal CO_2 contribution. During nighttime, on the other hand, MLTI CO_2 4.3 μm emission is orders of magnitude less than its daytime value. Consequently, analysis of the nighttime SABER 4.3 μm channel measurements enables the $NO^+(v)$ contribution to be separated reliably from the background $CO_2(v_3)$ contribution over a broad dynamic range of geomagnetic storm conditions, a feature necessary for developing an empirical storm-time response to geomagnetic activity (Mertens et al., 2007a,b). Therefore, the nighttime SABER 4.3 μm limb radiance measurements are used to derive $NO^+(v)$ VER, which provides an observation-based proxy to characterize the E-region response to solar-geomagnetic disturbances. Additional observational support for the plausibility of using $NO^+(v)$ 4.3 μm VER as an E-region proxy is presented in Section 2.1. The method of deriving vertical profiles of $NO^+(v)$ 4.3 μm VER from SABER limb radiance measurements is discussed in Sections 2.2 and 2.3.

2.1. Particle precipitation and auroral 4.3 μm emission

Auroral $NO^+(v)$ 4.3 μm emission is a prompt indicator of the ionosphere–thermosphere response to particle precipitation. This is observed by comparing outgoing ionosphere–thermosphere $NO^+(v)$ 4.3 μm radiative flux with incoming auroral electron energy flux, as shown in Fig. 1 for 4 days during large geomagnetic storm periods. The particle and radiative flux quantities selected for comparison were based on a spatial-temporal coincidence criteria of being within 2 deg in magnetic latitude and within 1.5 h in UT-time. The flux

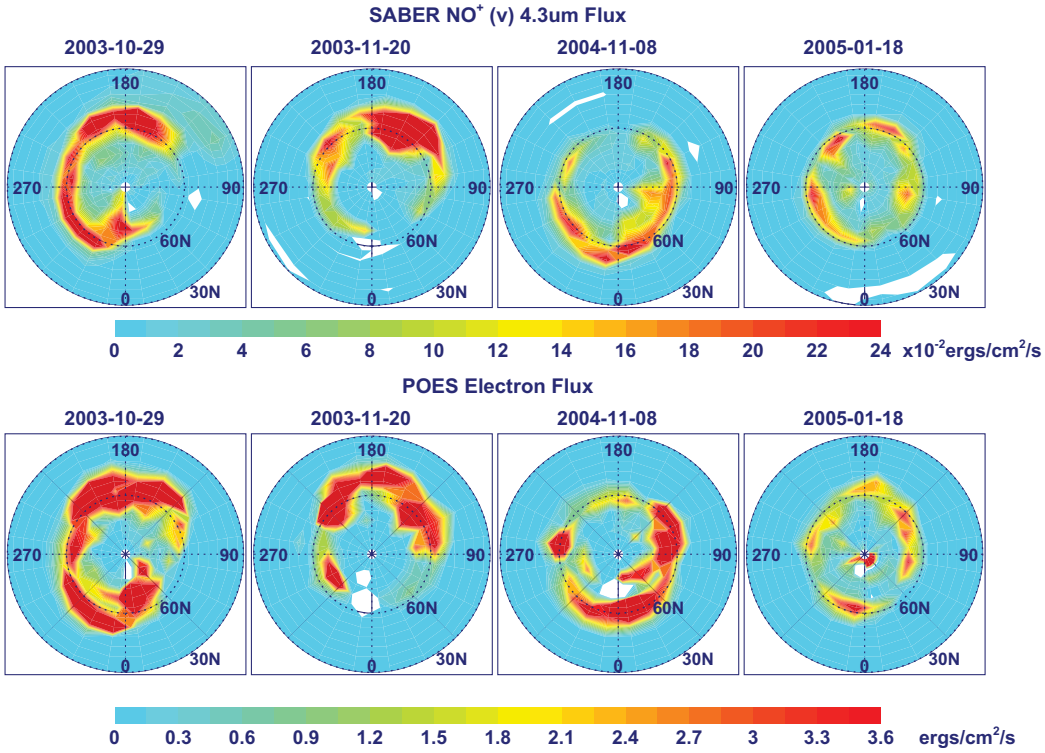

Fig. 1. The top row is total outgoing ionosphere–thermosphere SABER-derived $NO^+(v)$ 4.3 μm radiative flux. The bottom row is NOAA/POES precipitating electron total energy flux. The flux data are averaged SABER-POES nighttime coincidence measurements during representative solar-geomagnetic storm periods of solar cycle 23. The 60-degree magnetic latitude circle is identified. Magnetic longitudes at 0, 90, 180, and 270-degrees are also labeled. See Section 2.1 for details on coincidence criteria and radiative flux computations.

quantities were further sorted into 5 × 18 deg magnetic latitude and magnetic longitude bins, respectively, for plotting purposes, and averaged over the nighttime data on the date indicated in the title of each panel in Fig. 1. The bottom row shows total precipitating electron energy flux (ergs $cm^{-2}\ s^{-1}$) derived from measurements taken by the National Oceanic and Atmospheric Administration (NOAA) Polar Orbiting Environment Satellites (POES). The POES low energy Total Energy Detector (TED) and Medium Energy Proton and Electron Detector (MEPED) instruments were used to derive the total electron energy flux. The top row shows the SABER-derived total outgoing ionosphere–thermosphere $NO^+(v)$ 4.3 μm radiative flux. Prior to computing averages of the SABER radiative flux data, individual profiles of $NO^+(v)$ 4.3 μm radiative flux F (ergs $cm^{-2}\ s^{-1}$) were computed by vertically integrating each SABER-derived $NO^+(v)$ VER V(z) (ergs $cm^{-3}\ s^{-1}$), such that

$$F = \int_{z_B}^{z_T} V(z)dz. \quad (1)$$

The radiative flux includes the contribution from all of the $NO^+(v)$ 4.3 μm vibration–rotation bands, which requires the SABER-derived $NO^+(v)$ 4.3 μm VER to be multiplied by an unfilter factor (Mlynczak et al., 2002). The unfilter factor is defined as the ratio of the total volumetric emission rate of radiative energy (all 4.3 μm vibration–rotation bands in this case) to the in-band volume emission rate measured by the SABER 4.3 μm radiometer channel (2290–2405 cm). Using model simulations of $NO^+(v)$ 4.3 μm emission, as described by Mertens et al. (2007a, 2008, 2009a), the unfilter factor was determined to be 3.5, roughly independent of altitude. As mentioned previously, the method of deriving the $NO^+(v)$ 4.3 μm VER is described in Sections 2.2 and 2.3.

The limits of integration in (1) are taken as $z_B = 100$ km and $z_T = 200$ km, which contains most of the outgoing ionosphere–thermosphere radiative emission from $NO^+(v)$. Recall from the introduction that the $NO^+(v)$ vibrational states are excited by exothermic ion-neutral chemical reactions. During geomagnetic storms, the magnitude and shape of the atmospheric ion density profiles are governed by the precipitating particle total energy flux and the characteristic energy, respectively. Moreover, the steady-state $NO^+(v)$ concentrations are a balance between production from exothermic ion-neutral chemistry and loss by radiative emission and collisional quenching. The combination of these processes yield a $NO^+(v)$ 4.3 μm VER profile that generally peaks in altitude between 105 and 110 km, with most of the outgoing radiative emission confined to altitudes between 100 and 200 km (Mertens et al., 2007a, 2008; Fernandez et al., 2010). This is evident from Fig. 2, which shows representative $NO^+(v)$ 4.3 μm VER during the Halloween 2003 storm period.

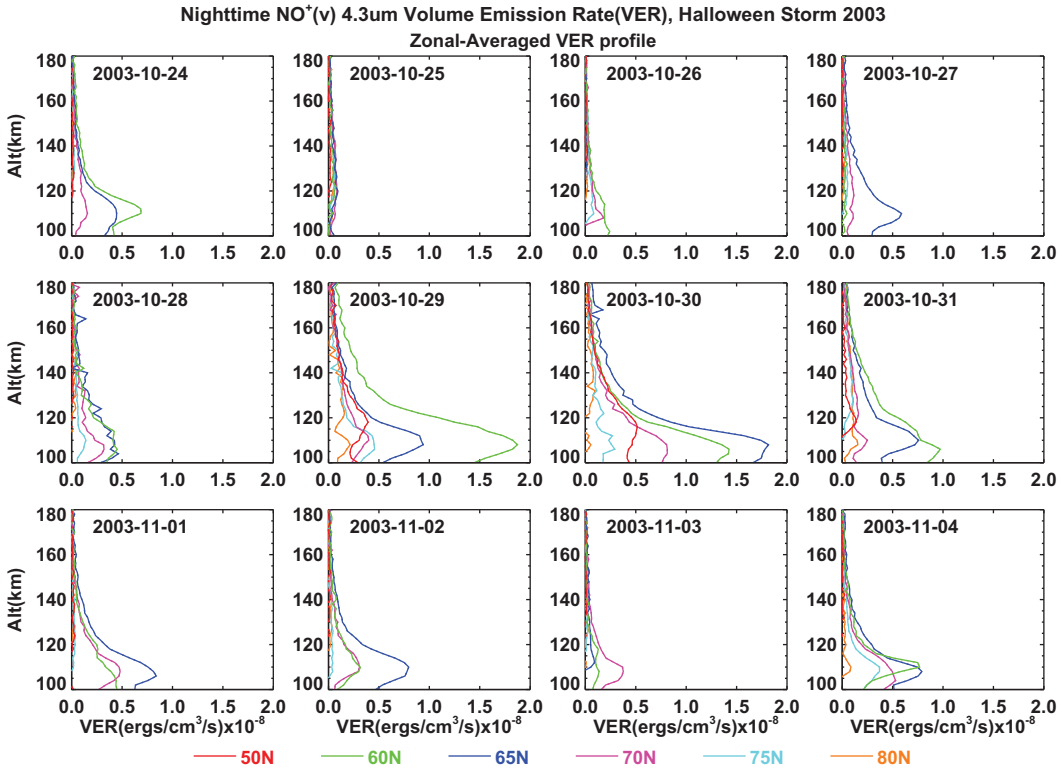

Fig. 2. Nighttime-averaged, zonal-mean $NO^+(v)$ 4.3 μm VER profiles during the Halloween 2003 storm period. The width of the indicated magnetic latitude bands is ±2.5 deg.

From the geomagnetic storm days shown in Fig. 1, it is clear that $NO^+(v)$ 4.3 μm emission responds to auroral dosing. The morphology of the outgoing ionosphere–thermosphere $NO^+(v)$ 4.3 μm radiative flux bears a striking resemblance to the patterns of auroral electron precipitation. There is one notable exception. The radiative flux on October 29, 2003 is enhanced at much lower latitudes than the particle flux between 90 and 180 deg magnetic longitude. The POES measurements show low latitude proton flux near 180 deg magnetic longitude (not shown). Although proton flux may contribute somewhat, cross correlation analysis of the SABER auroral radiative emissions strongly support chemical–dynamical processes as the cause of the low latitude storm-time enhancement in the $NO^+(v)$ 4.3 μm radiative flux (Mertens et al., 2007b, 2009b; Fernandez et al., 2010). That is, NO is transported out the auroral region to lower latitudes and the $NO^+(v)$ 4.3 μm emission is enhanced by the $O_2^+ + NO$ charge transfer reaction (Mertens et al., 2008).

The relationship between the radiative and particle flux is quantified by plotting nightly-averaged, zonal-mean NOAA/POES total electron energy flux versus SABER-derived $NO^+(v)$ 4.3 μm radiative flux for magnetic latitude bands that overlap the auroral oval region and for seven solar-geomagnetic storm periods. These results are shown in Fig. 3. The correlation coefficient between the particle and radiative flux data during each storm period varies between 0.83 and 0.94. Note that both northern and southern hemispheric storm data are shown in Fig. 3. The gradients in Fig. 3 fall within the gradient error envelope, as determined from the fitting algorithm. No doubt, analysis of more storm periods would reduce gradient error envelope. Fig. 4 combines the data from all the storm periods shown in the previous plot. By combining these data, the correlation coefficient between auroral electron precipitating energy flux and outgoing ionosphere–thermosphere $NO^+(v)$ 4.3 μm radiative flux is 0.88.

The POES and SABER observations presented in this section strongly support the conjecture that nighttime $NO^+(v)$ 4.3 μm emission is a suitable proxy for characterizing the auroral zone E-region response to solar-geomagnetic disturbances. In particular, the explicit observation-based proxy used to develop the STORM-E model is the nighttime $NO^+(v)$ 4.3 μm VER. The following two subsections describe the algorithms and methodologies used to derive this quantity from SABER 4.3 μm limb emission measurements.

2.2. Removal of $CO_2(v_3)$ contribution from SABER 4.3 μm measurements

$NO^+(v)$ VER is derived from SABER 4.3 μm limb emission measurements by (1) removing the background contributions of $CO_2(v_3)$ emissions from the measured 4.3 μm limb radiance, and (2) performing an Abel inversion on the subsequent residual limb radiance (i.e., measured – $CO_2(v_3)$ contributions) to obtain vertical profiles of $NO^+(v)$ VER. In this section, the method of obtaining the residual limb radiance is described.

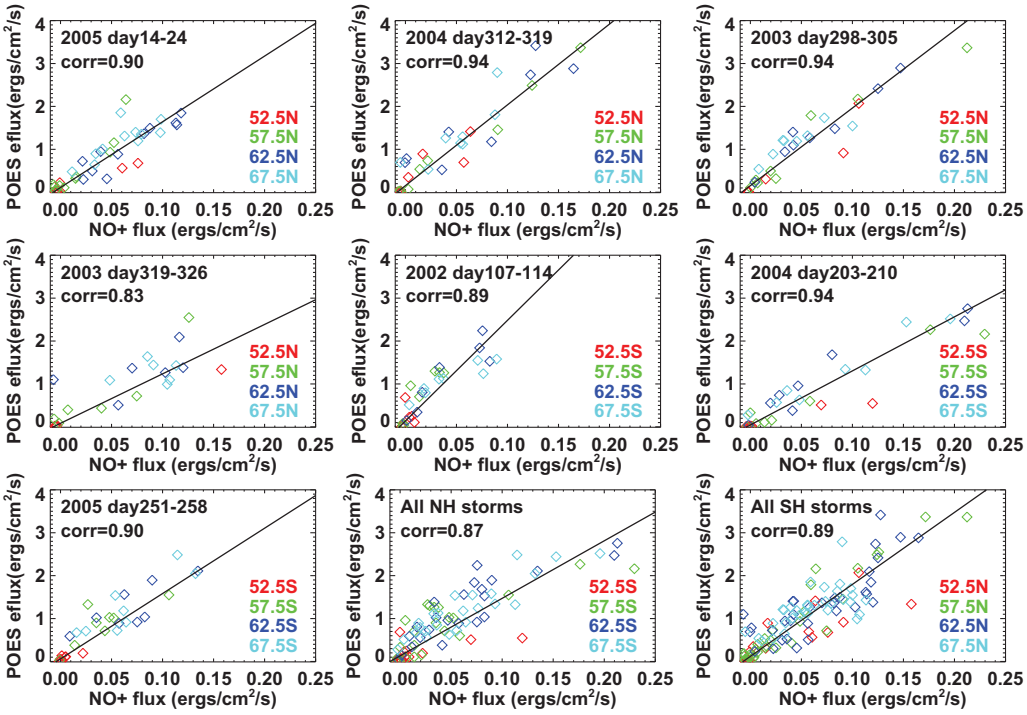

Fig. 3. Scatter plots of nighttime-averaged, zonal-mean NOAA/POES precipitating total electron energy flux versus SABER-derived $NO^+(v)$ 4.3 μm radiative flux for high-latitude magnetic latitude bands. These scatter plots are shown for seven solar-geomagnetic storm periods and the linear correlation coefficient between the particle and radiative flux data are indicated in the legends. Scatter plots for the seven storm periods are combined and separated into northern and southern hemisphere data in the last two columns of the bottom row.

The atmospheric radiance observed by the SABER 4.3 μm broadband radiometer can be modeled by the spectrally-integrated solution of the infrared radiation transfer equation for limb-viewing geometry (Goody and Yung, 1989), such that

$$R_{\Delta v}(z_T) = \sum_i \int_{x_s}^{x_{obs}} \int_{\Delta v} J_i(v,x;z_T) \frac{\partial \tau_i(v,x;z_T)}{\partial x} \Phi(v) dv dx, \qquad (2)$$

where x is the position along the limb line-of-sight (LOS) between the satellite observation point (x_{obs}) and a point at the furthest extend of the limb (x_s). The tangent altitude and wavenumber variables are denoted z_T (km) and v (cm^{-1}), respectively. The normalized spectral response function of the SABER 4.3 μm channel is represented by $\Phi(v)$ (unitless), and the integration over wavenumber is performed over the spectral width of the radiometer channel (2290–2405 cm). The radiative source function and transmittance are denoted $J_i(v,x;z_T)$ ($W/(m^2\ sr\ cm^{-1})$) and $\tau_i(v,x;z_T)$ (unitless), respectively, and the summation is over each ith vibration–rotation band that emits within the 4.3 lm channel spectral bandpass. The monochromatic transmittance along the LOS for the ith vibration–rotation band is given by

$$\tau_i(v,x;z_T) = \exp\left(-\int_x^{x_{obs}} k_i(v,s,z_T) N(s,z_T) ds\right). \qquad (3)$$

Here $k_i(v,s,z_T)$ (cm^2/molecules) is the molecular absorption coefficient for the ith vibration–rotation band and $N(s,z_T)$ (molecules/cm^3) is the total number density of absorbing molecules, which is taken to be CO_2 in this section. The absorption coefficient can be written in terms of the spectral line strength $S_{t_i}(x;z_T)$ (cm^2/(molecules $(cm^{-1})^{-1}$)) and the normalized spectral line shape function $g(v,v_{t_i})$ ($(cm^{-1})^{-1}$). Thus,

$$k_i(v,x;z_T) = \sum_{t_i} S_{t_i}(x;z_T) g(v,v_{t_i},x;z_T), \qquad (4)$$

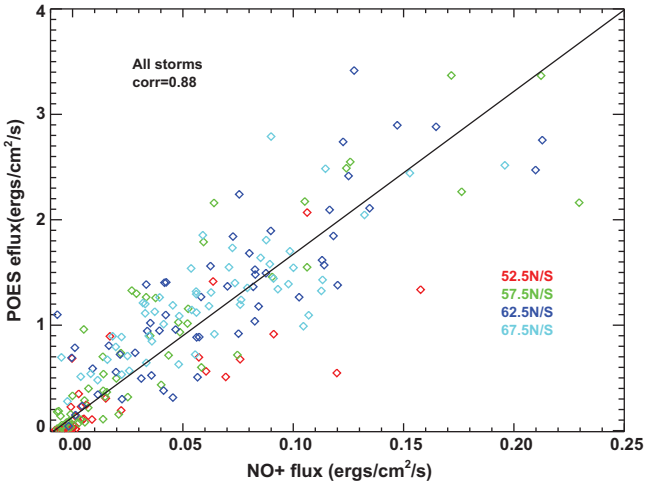

Fig. 4. Scatter plot of nighttime-averaged, zonal-mean NOAA/POES precipitating total electron energy flux versus SABER-derived $NO^+(v)$ 4.3 μm radiative flux for high-latitude magnetic latitude bands. This figure combines data from all the storm periods in the previous plot, independent of whether the data are from the northern or southern hemisphere.

where the sum in (4) is over all radiative vibration–rotation transitions that emit within the ith vibration–rotation band.

The methodology of calculating the $CO_2(v_3)$ contribution to the SABER 4.3 μm limb radiance measurements is to numerically solve (2) using the 4.3 μm forward radiance model component of the SABER operational non-local thermodynamic equilibrium (non-LTE) kinetic temperature (Tk) and CO_2 volume mixing ratio (vmr) retrieval algorithm, with atmospheric input data obtained from the routine SABER data products (Mertens et al., 2001, 2002, 2004, 2009a,c). The nighttime $CO_2(v_3)$ contributions that emit within the SABER 4.3 μm channel spectral bandpass arise from eight vibrational emission bands: the major isotopic ($^{16}O^{12}C^{16}O$) fundamental band, first hot band, and three second hot bands; and three minor isotopic ($^{16}O^{13}C^{16}O$, $^{16}O^{12}C^{18}O$, and $^{16}O^{12}C^{17}O$) fundamental bands. Thus, the summation in (2) includes these eight vibration–rotation bands. However, the radiative source functions and the transmittances for each emission band, which embody the microphysical properties of atmospheric emission and absorption, respectively, must be known prior to solving the spectrally-integrated LOS infrared radiation transfer equation in (2).

MLTI $CO_2(v_3)$ emissions are in vibrational non-LTE (Lopez-Puertas et al., 1986a,b; Nebel et al., 1994). Thus, the radiative source functions and the transmittances for each of the ith vibration–rotation bands in (2) are functions of the upper-level and lower-level vibrational state densities for the radiative transitions that emit in the 4.3 μm spectral region. For these non-LTE emissions, the vibrational state densities depend explicitly on the chemical, collisional, and radiative processes that excite and de-excite each vibrational state. The so-called non-LTE CO_2 model obtains the CO_2 vibrational state densities by simultaneously solving the coupled steady-state statistical equilibrium equations for the relevant vibrational states, and the infrared radiative transfer equations that radiatively couple the vibrational states to the ground-state or to each other. These coupled sets of equations are solved using the Modified Curtis Matrix approach (Lopez-Puertas et al., 1986a,b, 1998). The calculation of the broadband LOS radiance in (2) and the vibrational band radiation transfer calculations within the non-LTE CO_2 model are performed using BANDPAK routines (Marshall et al., 1994). BANDPAK solves the spectrally-integrated infrared radiation transfer equation along a specified viewing path by combining path-integrated composite emissivities, utilizing a database of pre-computed emissivity tables. The emissivity table databases are computed line-by-line using LINEPAK routines (Gordley et al., 1994). The non-LTE CO_2 model used in this analysis is largely based on the non-LTE CO_2 model used in the operational SABER Tk/CO_2 retrieval algorithm (Mertens et al., 2001, 2002, 2004, 2009c). However, accurate modeling of nighttime $CO_2(v_3)$ emissions required an important addition to the nominal SABER non-LTE CO_2 model, which is described in more detail below.

The main source of atmospheric input data below 120 km is SABER routine v1.06 data products. These input data are needed in the calculation of radiative source functions and the transmittances, and for the computation of the broadband LOS radiance in (2). The Tk and pressure data used are retrieved data products from the SABER measurements and are available in the SABER Level 2 data file. The source of CO_2 vmr data is a climatological database developed from the daytime simultaneous Tk/CO_2 retrieval data products (Mertens et al., 2009c). Daytime SABER-retrieved CO_2 vmr profiles are interpolated onto a fixed pressure grid and sorted and averaged as a function of latitude and season. Since diurnal variations in CO_2 are expected to be small, this CO_2 vmr database is used in the nighttime $CO_2(v_3)$ LOS radiance calculations. Other atmospheric input data required by the non-LTE CO_2 model are the main MLTI neutral species concentrations: N_2, O_2, and $O(^3P)$. These data are also included in the SABER Level 2 data file, which originate from the NRLMSIS-00 model (Picone et al., 2002).

The SABER atmospheric input data described in the previous paragraph are extended above 120 km using the NRLMSIS-00 model. The thermospheric temperature above 120 km in the NRLMSIS-00 model is based on the Bates–Walker representation (Picone et al., 2002). The Bates–Walker representation is an analytical solution for thermospheric temperature as a function of altitude, which is parameterized by the exospheric temperature at the upper boundary and by the global mean temperature at the 120 km lower boundary. The exospheric temperature is expressed as a function of geographical parameters and solar/magnetic indices (F10.7, 81-day average of F10.7, and Ap). The temperature at the 120 km lower boundary is represented by

$$T_{120} = \bar{T}_{120}[1 + G_{120}(L)], \tag{5}$$

where the overbar represents a global and temporal mean. The function $G(L)$ includes time-dependent terms, spherical harmonic terms, time-dependent lower-order harmonic terms, and polynomial terms in solar/magnetic activity. The approach used to extend the SABER temperature profile using the NRLMSIS-00 model is to replace the lower-boundary temperature in the Bates–Walker thermospheric temperature representation, i.e., T_{120} in (5), with the retrieved SABER Tk at 120 km for each SABER measurement scan used in the analysis. To improve stability, since the uncertainty in the retrieved SABER Tk at 120 km is quite high (see Mertens et al., 2001, 2004 for a discussion of the sources of uncertainty), the SABER temperature profile is averaged 5 km above and below the altitude closest to 120 km. The averaged-120 km SABER kinetic temperature is then input into the NRLMSIS-00 model to supply the lower-boundary condition, and the Bates–Walker representation is used to extend the SABER temperature profile to 200 km. The composition data

(N_2, O_2, and $O(^3P)$) is extended from 120 to 200 km using the NRLMSIS-00 model as well. The composition profiles generated from NRLMSIS-00 above 120 km are scaled to match the profiles contained in the SABER Level 2 data at 120 km.

Once the SABER temperature and composition data have been extended from 120 to 200 km using the NRLMSIS-00 model, the pressure profile is rebuilt, starting from the lowest altitude in the SABER Tk(p) profile (~12–15 km), using the barometric law and including the altitude dependence of the mean-molecular mass in a self-consistent iterative scheme. The SABER-derived climatological CO_2 vmr profiles are interpolated in log-pressure to the updated pressure profiles described above. This procedure for extending the SABER routine and climatological data products to 200 km is performed for each simulation of the $CO_2(v_3)$ contributions to the nighttime SABER 4.3 μm limb radiance measurements.

A significant source of nighttime CO_2 4.3 μm emission originates from energy transfer from vibrationally excited OH (i.e., OH($v \leqslant 9$)) to $N_2(1)$ by collisional quenching, which is subsequently transferred to the $CO_2(v_3)$ states by a V–V exchange mechanism (Lopez-Puertas et al., 1986b; Lopez-Puertas et al., 2004). The influence of this excitation process extends well above the OH layer due to the non-LTE process of local excitation (OH($v \leqslant 9$) → $N_2(1)$ → $CO_2(v_3)$) followed by radiative loss and re-absorption at higher altitudes. This energy transfer mechanism accounts for 20–40% of the nighttime $CO_2(v_3)$ 4.3 μm limb radiance from about 70 km to over 120 km (Lopez-Puertas et al., 2004). The OH($v \leqslant 9$) states are computed by combining an OH(v) kinetics model with the total chemical production rate of OH($v \leqslant 9$) determined from the OH(v) VER data product derived from SABER 2.0 μm channel limb radiance measurements, using the approach of Mlynczak et al. (1998). The method of calculating the rate of production of $N_2(1)$ from OH(v) was adopted from Lopez-Puertas et al. (2004). Incorporating this source of nighttime $CO_2(v_3)$ 4.3 μm emission represents a significant update to the nominal operational SABER non-LTE CO_2 model (Mertens et al., 2009a,c).

The above paragraphs presented an overview of the algorithms and methodologies employed in simulating nighttime $CO_2(v_3)$ 4.3 μm limb radiance. These techniques can be assessed by comparing $CO_2(v_3)$ 4.3 μm limb emission calculations with SABER 4.3 μm channel measurements during quiescent conditions ($kp \leqslant 3$). A large statistical ensemble of zonal-mean comparisons have been carried out for all seasons and for pole-to-pole latitudinal coverage (Mertens et al., 2009c). On average, the nighttime MLTI $CO_2(v_3)$ 4.3 lm limb radiance calculations generally agree with the corresponding SABER measurements to within 20% (Mertens et al., 2007a), as shown for quiescent equinox conditions in Fig. 5.

Once the nighttime $CO_2(v_3)$ 4.3 μm limb radiance is calculated, using the algorithms and methodologies described above, the SABER 4.3 μm residual limb radiance is obtained by

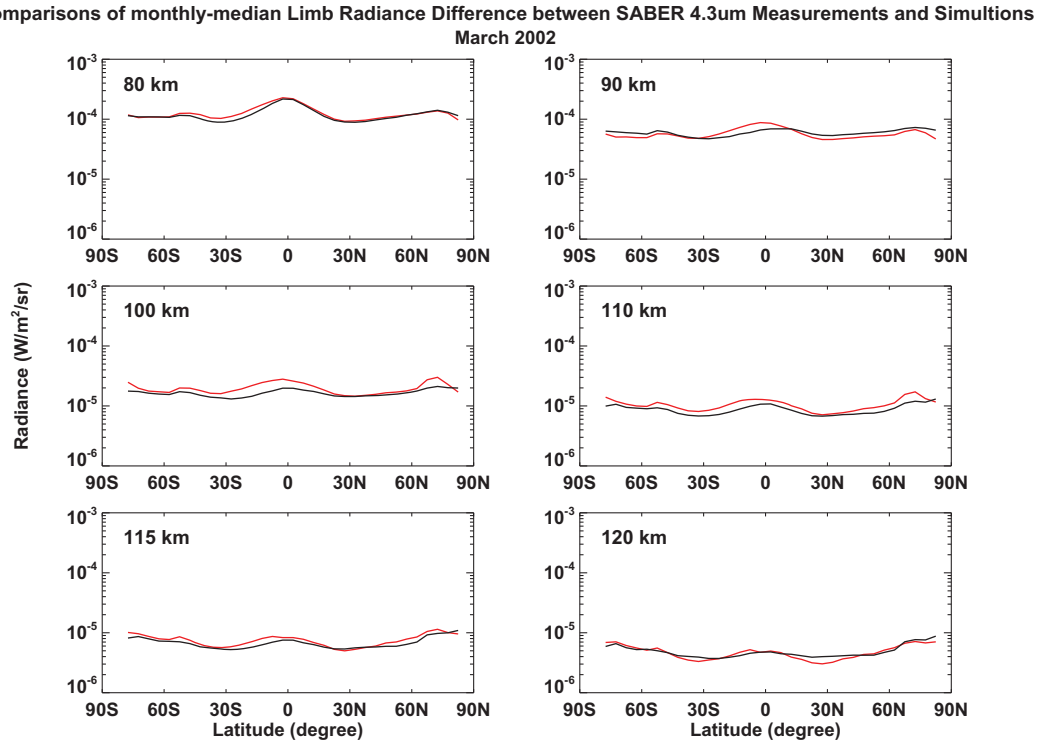

Fig. 5. Monthly zonal-median 4.3 μm limb radiance comparisons for quiescent conditions ($kp \leqslant 3$) during March 2002. The black solid lines are the SABER measurements. The red solid lines are the non-LTE $CO_2(v_3)$ simulations described in Section 2.2. (For interpretation of the references to color in this figure legend, the reader is referred to the web version of this article.)

$$\delta R_{\Delta\nu}(z_T) = R^{\mathrm{Meas}}_{\Delta\nu}(z_T) - R^{\mathrm{CO_2}}_{\Delta\nu}(z_T). \quad (6)$$

During geomagnetic activity, the residual 4.3 μm radiance is due to $NO^+(v)$ emission. This is affirmed by the statistical correlations between the SABER-derived $NO^+(v)$ 4.3 μm radiative flux and the precipitating particle flux (i.e., Figs. 1, 3, and 4), and explicit physics-based simulations of $NO^+(v)$ 4.3 μm emission (Mertens et al., 2007a, 2008, 2009a).

The broadband LOS radiative transport equation in (2) can be simplified for $NO^+(v)$ emission since $NO^+(v)$ 4.3 μm radiation transfer is optically thin at all altitudes (Winick et al., 1987a,b). Under weak-line, or optically thin, conditions the transmittance in (3) is approximated by

$$\tau_i(v,x;z_T) \approx 1 - \int_x^{x_{obs}} k_i(v,s,z_T)N(s,z_T)ds \quad (7)$$

and

$$\frac{\partial \tau_i(v,x;z_T)}{\partial x} \approx k_i(v,x;z_T)N(x,z_T). \quad (8)$$

In this case, the sum over the i-index includes the four $NO^+(v)$ vibration–rotation bands that emit within the SABER 4.3 μm channel spectral bandpass (Mertens et al., 2009a), and $N(s,z_T)$ is the total number density of NO^+. Substitute (2) into (6) using (8) and (4). The result is

$$\delta R_{\Delta\nu}(z_T) \approx \sum_i \int_{x_s}^{x_{obs}} \int_{\Delta\nu} J_i(v,x;z_T)k_i(v,x;z_T)N(x,z_T)\Phi(v)dvdx \quad (9)$$

$$\approx \sum_i \sum_{t_i} \int_{x_s}^{x_{obs}} \int_{\Delta\nu} J_i(v,x;z_T)S_{t_i}(x;z_T)g(v,v_{t_i},x;z_T) \times N(x,z_T)\Phi(v)dvdx. \quad (10)$$

By substituting the microphysical expressions for the radiative source functions and absorption coefficients into (10) (Lopez-Puertas et al., 1986a,b; Wintersteiner et al., 1992), the broadband limb radiance in the weak-line limit can be written as a LOS integral over the VER, such that

$$\delta R_{\Delta\nu}(z_T) \approx \frac{1}{4\pi}\int_{x_s}^{x_{obs}} V(x;z_T)dx, \quad (11)$$

where the VER is given by

$$V(x;z_T) = \sum_i \sum_{t_i} hc\nu_{t_i}A_{t_i}n_{u_{t_i}}(x;z_T)\int_{\Delta\nu} g(v,v_{t_i},x;z_T)\Phi(v)dv. \quad (12)$$

In the above equation, h and c are Planck's constant and the speed of light, respectively. The Einstein A-coefficient for the radiative transition t_i within the ith vibration–rotation band is denoted A_{t_i}; and $n_{u_{t_i}}(x;z_T)$ designates the upper vibrational state number density of NO^+ for the radiative transition labeled by t_i.

An additional approximation can be applied to the expression for the VER in (12). Generally, the normalized instrument spectral response function ($\Phi(v)$) varies slowly over the spectral width of a single radiative vibration–rotation transition in the MLTI region. As a result, (12) can be approximated by

$$V(x;z_T) \approx \sum_i \sum_{t_i} hc\nu_{t_i}A_{t_i}n_{u_{t_i}}(x;z_T)\Phi(\nu_{t_i}). \quad (13)$$

Evaluating the $NO^+(v)$ 4.3 μm VER from (13) requires a detailed understanding of the ion-neutral chemistry, and the collisional and radiative processes that excite and de-excite each ith vibration–rotation band that emits within the SABER 4.3 μm channel spectral bandpass, along with the corresponding chemical, kinetic, and spectroscopic parameters. The advantage of the SABER measurements is that the $NO^+(v)$ 4.3 μm VER can be obtained by inverting the weak-line LOS integral radiation transfer equation in (11), without knowledge of the physics and chemistry of $NO^+(v)$ energetics. The method of solving (11) for the $NO^+(v)$ VER, given the SABER 4.3 μm residual limb radiance profile, is discussed in the next section.

2.3. Deriving $NO^+(v)$ 4.3 μm volume emission rates

This section describes the second and final step in deriving $NO^+(v)$ VER from SABER 4.3 μm limb emission measurements. The first step is to obtain the 4.3 μm residual limb radiance by removing the $CO_2(\nu_3)$ contributions from the SABER 4.3 μm limb emission measurements using the algorithms and methods discussed in the previous section. The significance of this step is that the SABER-observed 4.3 μm residual radiance is identified with the LOS integral of the $NO^+(v)$ VER, as expressed in (11). The final step is to invert the integral equation in (11) in order to obtain the $NO^+(v)$ VER profile, given that the 4.3 μm residual limb radiance is known a priori.

The $NO^+(v)$ 4.3 μm VER is assumed to be symmetric about the tangent height z_T such that (11) is approximated by

$$\delta R_{\Delta\nu}(z_T) \approx \frac{C}{2\pi}\int_0^{x_{obs}} V(x;z_T)dx. \quad (14)$$

In the above equation, a unit conversion factor C has been introduced. The SABER-observed residual 4.3 μm limb radiance ($\delta R_{\Delta\nu}(z_T)$) is in units of W/(m^2 sr). Distance along the LOS (x) is in units of km. The volume emission rate is chosen to be given in units of ergs/(cm^3 s). As a result, $C = 100$ in order to covert (km ergs cm^{-3} s^{-1}) to (W m^{-2} sr^{-1}).

The integral over the LOS path (x) in (14) is converted to an integral over radial distance $R(z)$, where $R(z)$ is the radial distance from the center of the earth at altitude z. Thus, (14) is equivalently expressed as

$$R_{\Delta\nu}(z_T) = \frac{C}{2\pi}\int_{R(z_T)}^{R(\infty)} K(R(z))V(R(z))dR(z), \quad (15)$$

where the kernel of the integral equation is given by

$$K(R(z)) = \frac{R(z)}{\sqrt{R^2(z) - R^2(z_T)}}. \quad (16)$$

An integral equation with the above form is known as an Abel integral equation (Arfken, 1985). The inversion of (15) and (16) is referred to as an Abel inversion. The Abel integral equation can be inverted analytically. However, the analytic solution requires computing derivatives of integral functions of the left-hand side of (14) (Arfken, 1985). This approach is numerically unstable in remote sensing applications since the left-hand side of (14) is obtained from (noisy) measurement data. An alternative approach is employed in this section, which is to develop a stable numerical inversion of the Abel integral equation.

To obtain a numerical solution, the Abel integral equation in (15) is discretized. Let the i-index label the tangent altitude and let the j-index label the radial distance above the radial distance at the tangent height, such that

$$(2\pi/C)\delta R_{\Delta v}(z_T) \equiv y(z_T) \rightarrow y(z_i) \rightarrow y_i \tag{17}$$

$$R(z_T) \rightarrow R_i \tag{18}$$

$$R(z) \rightarrow R_j \tag{19}$$

$$R(\infty) \rightarrow R_\infty. \tag{20}$$

Incorporating the above definitions, (15) and (16) become

$$y_i = \int_{R_i}^{R_\infty} K_i(R)V(R)dR, \tag{21}$$

where the kernel is now given by

$$K_i(R) = \frac{R}{\sqrt{R^2 - R_i^2}}. \tag{22}$$

Define the integral on the right-hand side of (21) as

$$I_i \equiv \int_{R_i}^{R_\infty} K_i(R)V(R)dR. \tag{23}$$

The integral in (23) can be divided into N sub-intervals such that

$$I_i = \sum_{j=i}^{N} I_{ij}, \tag{24}$$

where

$$I_{ij} = \int_{R_j}^{R_{j+1}} K_i(R)V(R)dR \tag{25}$$

and R_N designates the highest altitude in the model atmosphere. Assume that the volume emission rate varies linearly through the sub-interval:

$$V(R) = a_j + b_j R, \quad (R_j \leqslant R \leqslant R_{j+1}). \tag{26}$$

Substituting (26) into (25) gives

$$I_{ij} = \int_{R_j}^{R_{j+1}} K_i(R)(a_j + b_j R)dR. \tag{27}$$

The constants a_j and b_j can be determined by the requirement that

$$V_j = a_j + b_j R_j \tag{28}$$

$$V_{j+1} = a_j + b_j R_{j+1}. \tag{29}$$

After deriving expression for the constants a_j and b_j from (28) and (29), and substituting them into (27), and grouping all terms proportional to V_j, the integrals in (24) and (25) can be expressed as a matrix–vector product. The result is

$$I_i = \sum_{j=i}^{N} I_{ij} = \sum_{j=i}^{N} A_{ij}V_j, \tag{30}$$

where V_j is the volume emission rate at the jth radial distance and the matrix elements A_{ij} are given by

$$\begin{aligned} A_{ij} = &-\frac{R_{j-1}}{R_j - R_{j-1}} \int_{R_{j-1}}^{R_j} K_i(R)dR + \frac{R_{j+1}}{R_{j+1} - R_j} \\ &\times \int_{R_j}^{R_{j+1}} K_i(R)dR + \frac{1}{R_j - R_{j-1}} \int_{R_{j-1}}^{R_j} K_i(R)RdR \\ &- \frac{1}{R_{j+1} - R_j} \int_{R_j}^{R_{j+1}} K_i(R)RdR. \end{aligned} \tag{31}$$

The four integrals in (31) can be evaluated analytically, given the expression for the kernel in (22). The final expression for the A_{ij} matrix elements is

$$\begin{aligned} A_{ij} = &\frac{R_{j-1}\left(\sqrt{R_{j-1}^2 - R_i^2} - \sqrt{R_j^2 - R_i^2}\right)}{R_j - R_{j-1}} \\ &+ \frac{R_{j+1}\left(\sqrt{R_{j+1}^2 - R_i^2} - \sqrt{R_j^2 - R_i^2}\right)}{R_{j+1} - R_j} \\ &+ \frac{R_j\sqrt{R_j^2 - R_i^2} - R_{j-1}\sqrt{R_{j-1}^2 - R_i^2}}{2(R_j - R_{j-1})} \\ &+ \frac{R_j\sqrt{R_j^2 - R_i^2} - R_{j+1}\sqrt{R_{j-1}^2 - R_i^2}}{2(R_{j+1} - R_j)} \\ &+ \frac{R_i^2}{2(R_j - R_{j-1})} \ln\left(\frac{R_j + \sqrt{R_j^2 - R_i^2}}{R_i}\right) \\ &- \frac{R_i^2}{2(R_j - R_{j-1})} \ln\left(\frac{R_{j-1} + \sqrt{R_{j-1}^2 - R_i^2}}{R_i}\right) \\ &+ \frac{R_i^2}{2(R_{j+1} - R_j)} \ln\left(\frac{R_j + \sqrt{R_j^2 - R_i^2}}{R_i}\right) \\ &- \frac{R_i^2}{2(R_{j+1} - R_j)} \ln\left(\frac{R_{j+1} + \sqrt{R_{j+1}^2 - R_i^2}}{R_i}\right). \end{aligned} \tag{32}$$

Combining (21), (23), (24), and (30), the discretized form of the Abel integral equation for weak-line LOS radiation transfer in (14) is expressed as

$$y_i = \sum_{j=i}^{N} A_{ij} V_j. \tag{33}$$

In matrix–vector notation, (33) can be written as

$$\mathbf{y} = \tilde{\mathbf{A}}\mathbf{V}. \tag{34}$$

The Abel integral equation in (14) is classified as a Fredholm integral equation of the first kind (commonly denoted IFK). Eq. (34) is a discretized IFK (denoted DKF). A unique, numerically stable solution to the DKF in (34) can be obtained using the Philips–Tikhonov–Twomey (PTT) regularization method (Phillips, 1962; Tikhonov, 1963; Twomey, 1963, 1977), which is the solution V_γ that minimizes the following expression

$$\min\left(\|\widetilde{\mathbf{A}}V - \mathbf{y}\|^2 + \gamma\|\widetilde{\mathbf{L}}(\mathbf{V} - \mathbf{V}_0)\|^2\right), \tag{35}$$

where $\widetilde{\mathbf{L}}$ is the matrix representation of the regularization (or smoothing) operator $\mathcal{L}$, which can be the identity operator, a first derivative, $\mathcal{L}V = V'$, a second derivative, $\mathcal{L}V = V''$, or any higher order derivative operator, etc. The vector $\mathbf{V}_0$ can be any specified mean-state, or zero. The solution to (35) is unique, and is formally given by

$$\mathbf{V}_\gamma = \left(\widetilde{\mathbf{A}}^T\widetilde{\mathbf{A}} + \gamma\widetilde{\mathbf{L}}^T\widetilde{\mathbf{L}}\right)^{-1}\left(\widetilde{\mathbf{A}}^T\mathbf{y} + \gamma\widetilde{\mathbf{L}}^T\widetilde{\mathbf{L}}\mathbf{V}_0\right). \tag{36}$$

The Lagrange multiplier γ is a constraint that ensures a unique, stable solution, and is closely related to the measurement errors (Twomey, 1977). An additional constraint imposed is that the vector norm of the measurement errors in $\mathbf{y}$ is bounded. If ϵ represents the errors in $\mathbf{y}$, then the constraint is

$$\sum_i \epsilon_i^2 = \delta^2. \tag{37}$$

An optimal solution is found by adjusting γ until the vector norm of the solution residual satisfies

$$r_\delta(\gamma) = \|\widetilde{\mathbf{A}}\mathbf{V}_\gamma - \mathbf{y}_\delta\| = \delta \pm \Delta\varepsilon, \tag{38}$$

where $\Delta\varepsilon$ is a pre-defined tolerance (e.g., 1%, 5% etc.). The algorithm steps are as follows:

1. Set $\gamma = \delta$.
2. Compute the solution from (36).
3. Compute the solution residual from (38).
4. If $\delta - \Delta\epsilon \leqslant r_\delta(\gamma) \leqslant \delta + \Delta\epsilon$, then STOP.
5. If $r_\delta(\gamma) < \delta - \Delta\epsilon$, then increase γ; goto 2.
6. If $r_\delta(\gamma) > \delta + \Delta\epsilon$, the decrease γ; goto 2.

In the inversion of SABER 4.3 μm residual limb radiance measurements in (14), the mean-state $NO^+(v)$ VER in (36) is assumed to be zero (i.e., $\mathbf{V}_0 = 0$), and the smoothing matrix operator $\widetilde{\mathbf{L}}$ is set equal to the second-order derivative operator (Twomey, 1977). Error analysis studies demonstrated that this constrained produces the minimum mean bias and statistical uncertainty in retrieved $NO^+(v)$ VER profiles.

This section completes the description of the algorithms and methodologies used to derive $NO^+(v)$ VER from SABER 4.3 μm limb emission measurements. The SABER-derived $NO^+(v)$ 4.3 μm VER is the observation-based proxy used to characterize the response of the E-region to solar-geomagnetic activity. The next section presents results from the $NO^+(v)$ VER retrieval algorithm and discusses important uncertainties.

3. Results and discussion

The purpose of the results presented in this section is threefold: (1) illustrate the fidelity and robustness of the numerical Abel inversion algorithm presented in Section 2.3, (2) quantify known sources of error in the $NO^+(v)$ VER retrieval algorithm, and (3) assess the influence of spatially structured emission sources on the 1-D Abel inversion. The results presented in this section provide important guidance in the development of the E-region peak electron density empirical storm-time correction factor presented in Part II of this series.

Fig. 6 demonstrates that the Abel inversion algorithm faithfully reproduces a known $NO^+(v)$ VER profile from a simulation of the corresponding SABER 4.3 μm channel limb radiance. The input atmospheric state and auroral dosing parameters were taken from the geomagnetic storm event studied by Mertens et al. (2008). The event was during the Halloween 2003 storm: October 30, 2003, 67N, 12E, and 1.69 UT. The reference $NO^+(v)$ VER profile (not shown) was computed by the $NO^+(v)$ chemical-kinetic model described in Mertens et al. (2007a, 2008, 2009a) using the input specifications for the aforementioned Halloween 2003 event. The non-LTE radiation transfer algorithms discussed in Section 2.2 were used to simulate the total ($CO_2(v_3)$ + $NO^+(v)$) limb radiance that, in principle, would be observed from the SABER 4.3 μm channel, which is shown in the left-hand column of Fig. 6. The figure also shows the separate contributions from $CO_2(v_3)$ and $NO^+(v)$. The Abel inversion algorithm was applied to the $NO^+(v)$ component of the SABER 4.3 μm channel limb radiance. The result is the $NO^+(v)$ VER profile shown in the right-hand column of Fig. 6, which exactly reproduces the reference $NO^+(v)$ VER profile (see Fig. 4 from Mertens et al., 2008). Recall that in practice, the $NO^+(v)$ contribution is derived by first modeling the $CO_2(v_3)$ component, which is subsequently subtracted from the measured (total) SABER 4.3 μm channel limb radiance, as described in detail in Section 2.2.

The above demonstration of the Abel inversion algorithm was a test under ideal conditions where the limb radiance was assumed to be known perfectly. Actual radiance measurements are subject to both systematic and random errors. The radiometric calibration error is less than 2% (Mertens et al., 2001). The largest systematic error in retrieving $NO^+(v)$ VER from SABER 4.3 μm channel limb radiance measurements arises from subtracting the

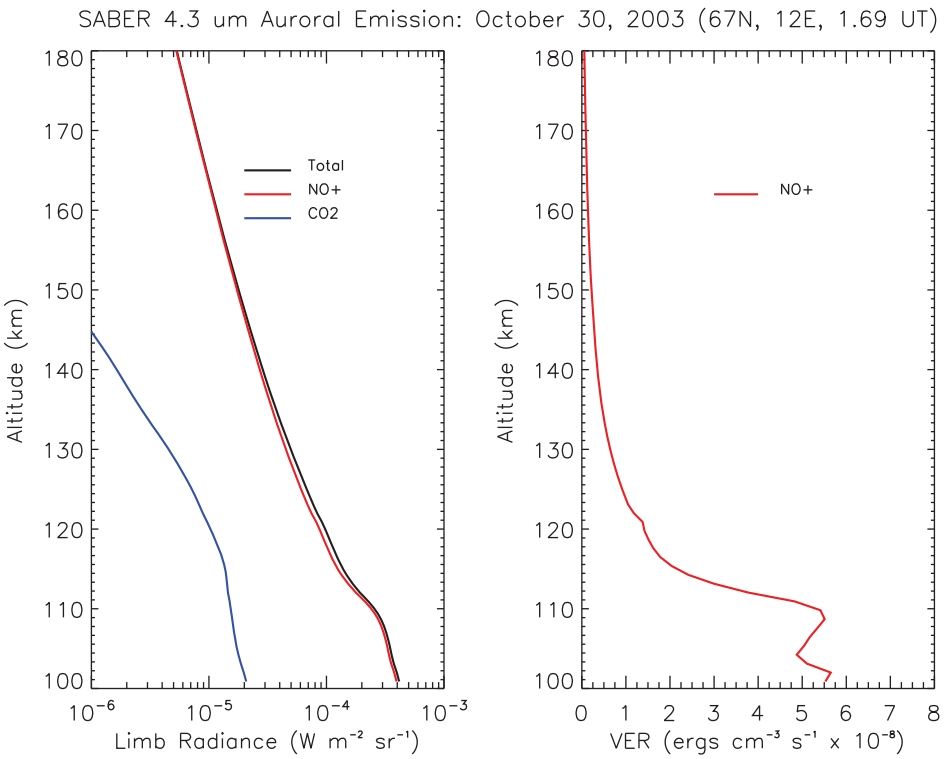

Fig. 6. Simulated SABER 4.3 μm limb radiance and the corresponding retrieved $NO^+(v)$ VER profile for the geomagnetic storm conditions on October 30, 2003 at 67N, 12E, and 1.69 UT. The limb radiance profile was computed using the $CO_2(v_3)$ model described in Section 2.2 and $NO^+(v)$ the chemical-kinetic model using the input atmospheric and auroral dosing conditions described in Mertens et al. (2008). The simulated SABER 4.3 μm channel limb radiance is shown in the left-hand column: $CO_2(v_3)$ contribution (blue), $NO^+(v)$ contribution (red), and total (black: $CO_2(v_3) + NO^+(v)$). The $NO^+(v)$ VER profile in the right-hand column was retrieved from the $NO^+(v)$ 4.3 μm limb radiance profile in the left-hand column using the numerical Abel inversion algorithm described in Section 2.3. (For interpretation of the references to color in this figure legend, the reader is referred to the web version of this article.)

modeled $CO_2(v_3)$ contribution from the measured radiance in order to obtain the $NO^+(v)$ contribution. The error in modeling the $CO_2(v_3)$ contribution was discussed previously in Mertens et al. (2007a). As shown in Section 2.2, the model simulations of quiescent nighttime 4.3 μm limb radiance, which is mainly due to $CO_2(v_3)$ emission, generally agree with SABER 4.3 μm channel limb radiance measurements to within 20%. From Mertens et al. (2007a), $CO_2(v_3)$ contributes 20–40% of the total SABER 4.3 μm limb emission during moderate auroral dosing conditions. Thus, the systematic modeling errors in simulating the $CO_2(v_3)$ contribution will introduce no more than 4–8% error in the retrieved $NO^+(v)$ VER profile under moderate geomagnetic storm conditions. The systematic error in the retrieved $NO^+(v)$ VER profile decreases with increasing geomagnetic activity.

Fig. 7 shows the influence of random errors on retrieved $NO^+(v)$ VER profiles. The source of random error is primarily electronic noise in the SABER 4.3 μm channel detector system. The noise equivalent radiance (NER) for the SABER 4.3 μm channel is 7.35×10^{-7} W m^{-2} sr^{-1}. Four reference VER profiles (not shown) were computed for different auroral dosing conditions using the $NO^+(v)$ chemical-kinetic model (Mertens et al., 2007a, 2008, 2009a). The corresponding simulated $NO^+(v)$ contributions to the SABER 4.3 μm channel limb radiances are shown for the four reference cases in the left-hand column of Fig. 7. These radiances are considered to be perfectly known and are indicated by the blue lines labeled 'No Noise'. Random Gaussian noise was added to the limb radiance at each altitude in Fig. 7. The standard deviation in the Gaussian noise distribution was specified by the SABER 4.3 μm channel NER. The noisy limb radiance profiles are indicated in the left-hand column of Fig. 7 by the green lines labeled 'Added Noise'. The $NO^+(v)$ VER profiles shown in the right-hand columns of Fig. 7 were retrieved from the noisy 4.3 μm limb radiance profiles shown in the left-hand column.

The $NO^+(v)$ VER profiles in Fig. 7 were retrieved from the noise-perturbed limb radiances under two conditions: unconstrained and constrained, which are indicated by the red and green lines, respectively. The unconstrained retrieval is characterized by setting the Lagrange multiplier γ in (36) to zero. Thus, there is no regularization, or smoothing, of the retrieved profile. This means that the noise in the limb radiance profile is undamped and mapped into the retrieved VER profile. Hence, the high-frequency vertical structure in the retrieved VER profile is not indicative of actual geophysical variation, but simply a manifestation of noise in the measured radiance. As the four cases

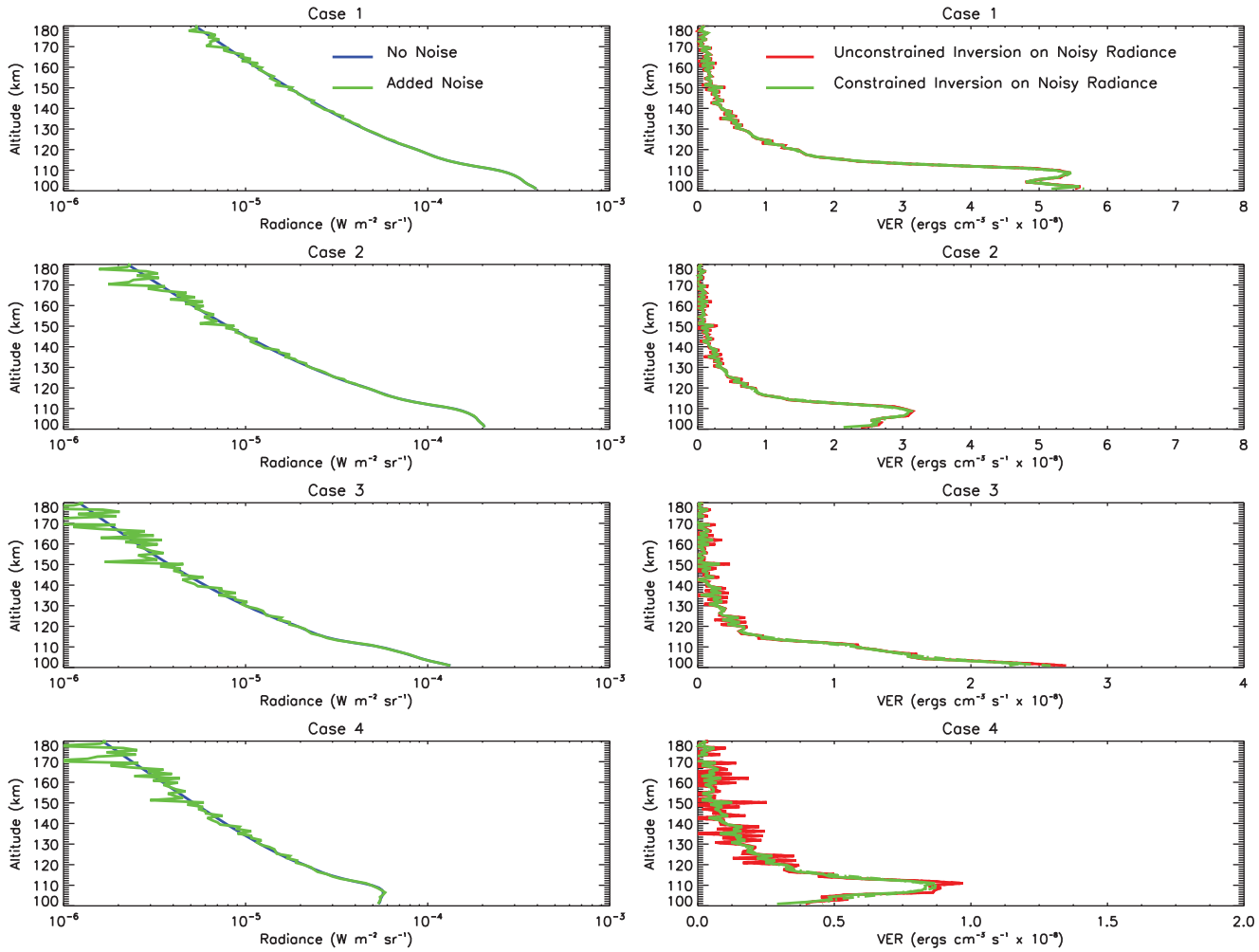

Fig. 7. Four cases of simulated SABER 4.3 μm channel limb radiances and corresponding $NO^+(v)$ VER Abel inversions. Reference $NO^+(v)$ VER profiles were computed using the chemical-kinetics model presented in Mertens et al. (2007a, 2008, 2009a) for a variety of auroral dosing parameters (not shown). SABER 4.3 μm channel limb radiance profiles were computed from the reference $NO^+(v)$ VER profiles and shown in the left-hand column as blue lines (labeled: no noise case). Random Gaussian noise was added to limb radiance profiles at each altitude using the SABER 4.3 μm channel noise equivalent radiance (NER) as the standard deviation in the Gaussian noise generator. The limb radiance profiles with realistic noise added as shown as green lines in the left-hand column labeled: added noise. The Abel inversion algorithm was applied to the noisy limb radiance profiles to derive the $NO^+(v)$ VER profiles, which are shown in the right-hand column. The $NO^+(v)$ VER profiles were derived using two parameter settings in the numerical Abel inversion algorithm: unconstrained (red lines) and constrained (green line). (For interpretation of the references to color in this figure legend, the reader is referred to the web version of this article.)

indicate in Fig. 7, the smaller the magnitude of the limb radiance the larger the effect of the measurement noise on the retrieved quantity. The constrained retrieval, on the other hand, regulates, or smooths, the retrieved VER profile by effectively requiring that the VER profile be adjusted by the inversion algorithm such that the simulated limb radiance at each tangent altitude is matched to the measured radiance at that altitude to within the uncertainty indicated by the specified measurement error. This is a pedagogical description of the role of the regularization operator $\tilde{\mathbf{L}}$ and Lagrange multiplier γ in (36). And in this application, the regularization operator is smoothing out high-frequency variations in the second-order derivatives of the $NO^+(v)$ VER profile, as discussed at the end of the previous section. Fig. 7 clearly shows that the constrained retrieval significantly suppresses the influence of noise in the limb radiance measurements on the retrieved VER profile. The trade-off with adding a constraint to dampen out noise variations is that biases can be introduced in resolving narrow peaks. This type of bias is seen in case 4 shown in Fig. 7, which is further quantified below.

A large ensemble of $NO^+(v)$ VER retrievals were performed on noise-perturbed limb radiances in order to quantify the effects of random measurement noise. The reference limb radiance profiles in Fig. 7 were perturbed by random Gaussian noise before retrieving the $NO^+(v)$ VER, as described in the previous paragraph. This step was repeated 100 times for each of the four cases in Fig. 7. The mean and standard deviation were computed from the ensemble of retrieved $NO^+(v)$ VER profiles. The

mean error was computed with respect to the reference VER profile. The mean error is indicative of systematic biases induced in the retrieved VER by noise in the measured limb radiances. The standard deviation represents the random uncertainty in a single $NO^+(v)$ VER retrieval due to random uncertainty in the measured SABER 4.3 μm limb radiance. The results of this study are shown in Fig. 8 for both the unconstrained and constrained retrievals.

The results from the error analysis described above and shown in Fig. 8 are summarized below. Since the $NO^+(v)$ VER data utilized in the development of the STORM-E model is confined to altitudes below 130 km (Mertens et al., submitted for publication), the discussion will also concentrate on this altitude range. The constrained versus unconstrained retrieval approach has a smaller effect on retrieved $NO^+(v)$ VER profiles for strong geomagnetic storms compared to weak to moderate geomagnetic activity. Case 1 represents strong geomagnetic activity. The absolute maximum bias in the unconstrained $NO^+(v)$ VER retrieval for altitudes less than 130 km is within 2%. For the constrained retrieval, the absolute maximum bias for altitudes less than 130 km is within 4%. At stated previously, the constrained retrieval can increase biases in resolving peaks in the VER profiles, such as the two peaks below 110 km for case 1 shown in Fig. 8. The maximum statistical uncertainty in the derived VER profile at altitudes below 130 km for case 1 is 11% for the unconstrained retrieval and 3% for the constrained retrieval. Even though the constrained retrieval approach increased the bias by a factor of two compared to the unconstrained approach, the constrained retrieval reduced the statistical uncertainty by nearly a factor of four.

The differences between the constrained and unconstrained retrieval approaches is more pronounced for weak to moderate geomagnetic disturbances, where noise in the limb radiance measurements has a larger effect on the retrieved VER profile. Consider case 4 in Fig. 8. The absolute maximum bias in the unconstrained retrieval for altitudes less than 130 km is within 7%. The absolute maximum bias below 130 km is also within 7% for the constrained retrieval. On the other hand, the constrained

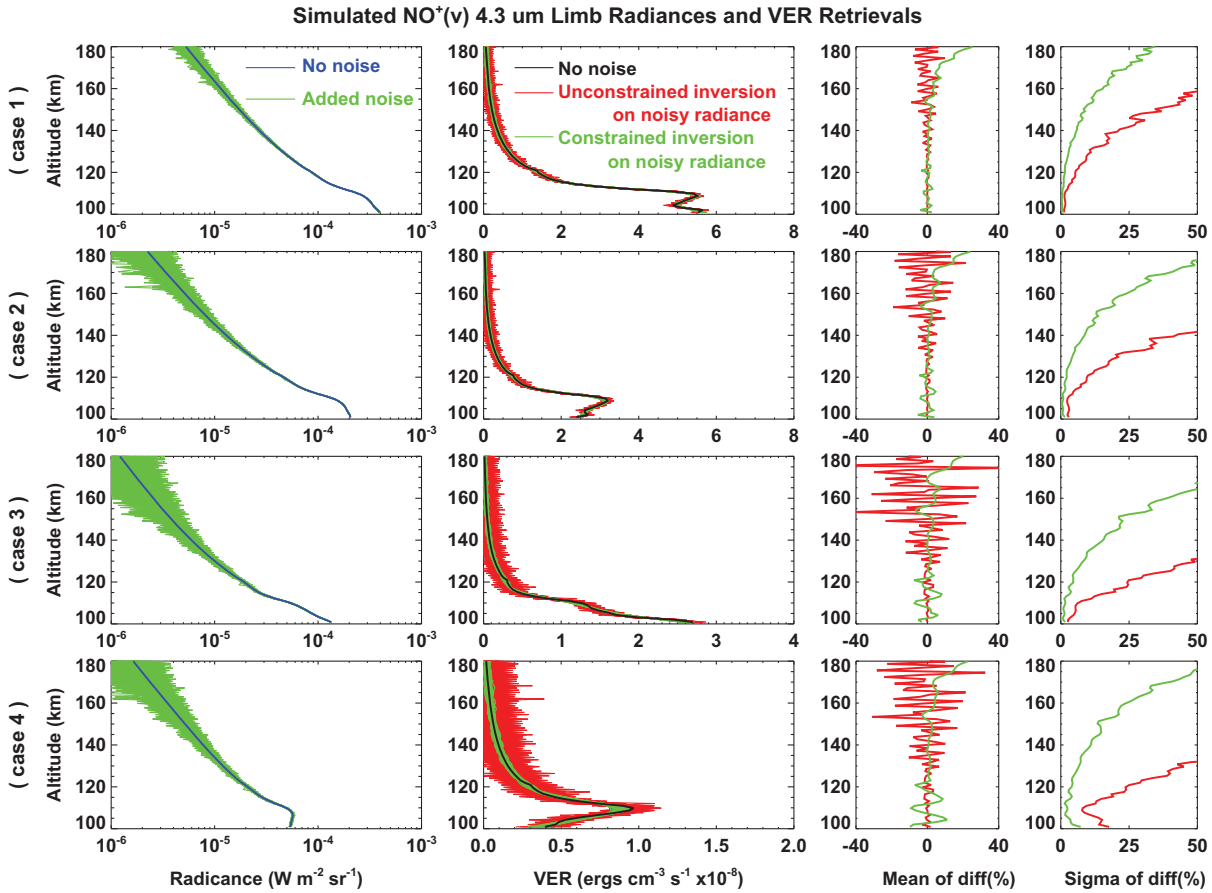

Fig. 8. Error assessment for the four case studies shown in the previous figure. For each case, an ensemble of $NO^+(v)$ VER retrievals were performed from noise-perturbed limb radiances. The ensemble size is $n = 100$. That is, for each case, the simulation of the SABER 4.3 μm channel limb radiance profile was perturbed by random Gaussian noise, with the standard deviation of the noise level given by the 4.3 μm channel NER. This was done n-times and the $NO^+(v)$ VER was retrieved for each realization of the noise-perturbed limb radiance profile. The fist column shows the limb radiance data, the second column shows the retrieved $NO^+(v)$ VER profiles, the last two columns show the mean error and standard deviation of the retrieved VER profiles with respect to the known reference VER profile.

retrieval reduced the statistical uncertainty by over a factor of six relative to the unconstrained retrieval. The maximum statistical uncertainty in the unconstrained VER retrieval at altitudes below 130 km for case 4 is within 45%, while the maximum statistical uncertainty is within 7% for the constrained retrieval approach.

The STORM-E model utilizes altitude-averaged $NO^+(v)$ VER data over the altitude range from 116 km to 120 km. The reasons for using altitude-averaged VER data over this altitude range are discussed by Mertens et al., submitted for publication. However, it is clear from Fig. 8 that averaging over altitude offers some benefit in reducing the errors in the retrieved $NO^+(v)$ VER, due to the effects of instrument noise in the SABER 4.3 μm limb radiance measurements. For strong auroral dosing represented by case 1 in Fig. 8, the absolute maximum bias in the altitude-averaged $NO^+(v)$ VER is within 3% for the unconstrained retrieval, and the statistical uncertainty is less than 2%. For the constrained retrieval, the absolute maximum bias in the altitude-averaged $NO^+(v)$ VER is on the order of 0.2%, while the statistical uncertainty is less than 1%. For case 4, which is representative of weak to moderate auroral activity, the absolute maximum bias in the unconstrained retrieval is within 14%, and the statistical uncertainty is within 6%. The absolute maximum bias in the constrained retrieval is on the order of 0.2%, while the statistical uncertainty is within 2%.

To summarize the error analysis and its relevance to the development of STORM-E, the SABER-derived $NO^+(v)$ VER data is based on the constrained Abel inversion algorithm with regularization applied to the second-order derivatives in the VER profile, as discussed at the end of Section 2.3. Since the STORM-E model uses altitude-averaged $NO^+(v)$ VER data over the altitude range from 116 km to 120 km, the error in this quantity, due to the influence of measurement noise in the SABER 4.3 μm limb emission observations, is effectively 1% in statistical uncertainty with a zero mean bias. Combined with 2% calibration error, and the maximum of 8% modeling error due to subtracting the $CO_2(\nu_3)$ contribution from the measured SABER 4.3 μm limb radiance, the root-mean-sum (RMS) error in the 116–120 km altitude-averaged $NO^+(v)$ VER for moderate geomagnetic storm conditions is 8%. Recall that for these sources of uncertainty, the RMS error decreases as geomagnetic activity increases.

The remainder of the results and discussion in this section are dedicated to assessing the influence of spatially structured emissions on the 1-D Abel inversion algorithm. The algorithm in Section 2.3 assumes that the emission source is spherically symmetric and varies linearly through an atmospheric layer. The vertical structure of the $NO^+(v)$ VER profile, as indicated by the $NO^+(v)$ chemical-kinetic model simulations (Mertens et al., 2007a, 2008, 2009a), suggest that the assumption of piece-wise linear variation of the emission rate through an atmospheric layer likely does not introduce large biases in the retrieved $NO^+(v)$ VER profile, except possibly near the peak at roughly 110 km. In the STORM-E model development presented in Part II, the empirical storm-time correction factor for the E-region peak electron density is derived from $NO^+(v)$ VER at altitudes between 116 and 120 km. Consequently, the assumption of piece-wise linear variation in emission rates at these altitudes is a reasonable approximation to the vertical inhomogeneity (see Fig. 2).

The more difficult assumption in the 1-D Abel inversion algorithm to assess, and to control its effects on the processing of the SABER limb radiance measurements in particular, is the assumption of a spherically symmetric emission source. Auroral emissions are known to be highly structured spatially (and temporally). Measurement strategies have been developed to account for high spatial variability in auroral emission observations from satellite-borne and rocket-borne platforms, such as adopting various spin scanning operating modes for the detector system in combination with tomographic techniques in the data inversion algorithms – e.g., see McDade and Llewellyn (1991) and Solomon et al. (1984). The imaging system and the cross-track scanning technique of the Global Ultraviolet Imager (GUVI) instrument aboard the TIMED satellite enables an approximate 7 × 7-km spatial resolution in nadir view, for example (Christensen et al., 2003). However, the SABER instrument was not designed to address the degree of horizontal inhomogeneity that may be present in auroral emissions. Therefore, the focus of the remaining discussion is to assess the influence of spatially structured $NO^+(v)$ emission on the VER retrieval from the 1-D Abel inversion algorithm. This study will provide guidance in identifying the effects of spatially structured $NO^+(v)$ auroral emission on the SABER-derived VER profiles.

The most important case for the analysis of SABER auroral emissions, by which an auroral emission source violates spherical symmetry, is to consider a horizontally localized emission source. In addition, with respect to satellite limb-view emission measurements, the horizontally localized emission source may not be symmetric about the tangent altitudes. Due to the long horizontal length of the tangent layer along the limb-view path, the effects of emission source localization along the limb-view direction will addressed. These effects will be assessed by comparing the retrieved VER profiles from simulated limb radiances from non-spherically symmetric emission sources, using the 1-D Abel inversion algorithm, with a reference VER profile that contains the same vertical structure as the non-spherically symmetric emission sources, but with a horizontal distribution that is consistent with a spherically symmetric emission source. All VER profiles used in this assessment are represented by the following analytical form:

$$V(z) = \sum_i V_{p_i}\, g_z(z; z_{p_i}, \sigma_{z_i}) g_\psi(\psi; \psi_{p_i}, \sigma_{\psi_i}) + V_o, \tag{39}$$

where g_z and g_ψ are unnormalized Gaussian functions of altitude z and angle ψ, respectively, and V_o is a constant background VER. The angle ψ is defined as the angle between the radial distance, with respect to the center of

the Earth, at the tangent altitude $R_T(z)$ and the radial distance at a position along the limb path $R(x)$ at a horizontal distance x from R_T(z). The peak altitude and standard deviation in the Gaussian altitude distribution g_z are denoted z_p and σ_z, respectively. Similar definitions hold for the Gaussian angular distribution g_ψ. The peak magnitude of the VER altitude–angular distribution is denoted by V_p.

Before proceeding further, some important geometric relations and derived quantities relevant to SABER limb-view observations are introduced. First, the radial distance along the horizontal limb path $R(x)$ is related to the radial distance at the corresponding tangent altitude $R_T(z)$ and the horizonal distance x with respect to $R_T(z)$ by

$$R(x) = \sqrt{R_T^2(z) + x^2}. \tag{40}$$

Second, given the definition of the angle ψ from the previous paragraph, this angle is related to the above three distance quantities by

$$\sin\psi = \frac{x}{R(x)} \tag{41}$$

and

$$\tan\psi = \frac{x}{R_T(z)}. \tag{42}$$

The vertical instantaneous field-of-view (IFOV) of the SABER 4.3 μm channel detector system is approximately 2 km. The width of the horizontal IFOV is roughly 35 km. The horizonal length of the tangent layer at 110 km is $x = \sim\pm160$ km, given an Earth radius R_e of 6360 km at high-latitude (i.e., 67N). Moreover, the horizontal half-length of the tangent layer makes an angle of $\psi = \pm1.42$ deg with respect to the radial distance at the tangent altitude. Thus, SABER routine data products at a tangent altitude of 110 km, for example, are derived from measurements of limb infrared radiance emitting from an atmospheric volume (length × width × height) of 320 × 35 × 2-km, where it is assumed that the horizontal length is centered about the tangent altitude. Similarly, the NO^+(v) VER derived from SABER 4.3 μm limb radiance measurements, using the 1-D Abel inversion algorithm, assumes that the auroral NO^+(v) emission source itself is independent of angle ψ, that the emission rate along the horizontal path is symmetric about the tangent altitude, and that the only variation in the emission rate is a piece-wise linear variation with altitude.

The largest horizontal distance x and angular extent ψ encountered in the NO^+(v) VER Abel inversion algorithm are the following. The highest altitude in the VER retrieval algorithm is 200 km. The lowest altitude is 80 km. The horizontal half-distance x of a 200 km altitude mapped onto a 80 km tangent altitude limb path is $\sim\pm1249$ km, which makes an angle ψ of ±10.5 deg with respect to the tangent altitude radial distance. The quantities derived in this paragraph provide important background and context for the discussion below.

The reference VER profile for the assessment of the effects of horizontally localized emission sources on the 1-D Abel inversion algorithm is given by (39) using the following parameter specification. The VER profile is a superposition of two terms in (39). The Gaussian altitude distribution in one term has a peak magnitude of 1×10^{-8} ergs cm^{-3} s^{-1} located at 130 km with an altitude spread given by a full-width half-max FWHM(z) of 5 km. The altitude distribution in the other term has a peak magnitude of 4×10^{-8} ergs cm^{-3} s^{-1} located at 110 km with an altitude spread given by a FWHM(z) of 10 km. The constant background V_o is set to 0.2×10^{-8} ergs cm^{-3} s^{-1}. This specified altitude distribution is similar to typical SABER-derived auroral NO^+(v) VER profiles but with some additional complexity, since actual NO^+(v) VER profiles normally have one vertical peak at around 110 km (see Fig. 2). The added complexity in the reference VER profile facilitates a more thorough analysis. The angular distributions for the two terms in the reference VER profile are identical. The peak angle is zero (i.e., $\psi_{p_i} = 0$) and the angular spread is given by a FWHM(ψ) of 100 deg. Since the largest angular extent encountered in the NO^+(v) VER retrieval algorithm is ±10.5 deg, as demonstrated in the previous paragraph, the FWHM(ψ) of 100 deg ensures that the emission sources are effectively independent of angle ψ, and the only variation in the emission rate is given by the specified altitude distribution. Thus, the simulated limb radiance from this reference VER profile will satisfy the spherically symmetric assumptions enumerated above.

The reference VER profile and simulated limb radiance are shown in Figs. 9, 10. The reference VER profile is shown as the black solid line labeled 'Synthetic VER' in Fig. 9. The projection of the reference VER profile onto the 130 and 110 km tangent altitude limb-view paths are shown in Fig. 11. For the 130 km tangent altitude in Fig. 11, the peak value of VER drops off with horizontal distance centered about the tangent location (i.e., $x = 0$) according to the projection of the altitude distribution of VER above the tangent altitude onto the limb path corresponding to the tangent altitude. For example, Fig. 9 indicates that the reference VER decreases to the constant $V_o = 0.2 \times 10^{-8}$ ergs cm^{-3} s^{-1} at around 137 km, which maps to a horizontal distance of ~±300 km along the 130 km tangent altitude limb path. Thus, the limb path VER distribution in Fig. 11 for the 130 km tangent altitude has reached the V_o value by roughly ±300 km, consistent with the geometric argument noted above. It is clear from Fig. 11 that the limb path VER distribution at 110 km tangent altitude has not reached the V_o value by ±300 km because the FWHM(z) for the peak in the altitude distribution at 110 km is 10 km in comparison to the FWHM(z) of 5 km for the peak in the altitude distribution at 130 km. The secondary peaks in the limb path VER distribution at the 110 km tangent altitude are a projection of the vertical peak at 130 km onto the 110 km tangent altitude limb path. Specifically, the projection of an altitude of 130 km

onto the limb path for a 110 km tangent altitude occurs at the horizontal length $x = \pm 510$ km, which is consistent with the limb path VER distribution shown in Fig. 11 for the 110 km tangent altitude. The limb radiance is determined from the limb path VER distribution by performing the line integral according to (11). The limb radiance corresponding to the reference VER distribution is shown in Fig. 10. If the 1-D Abel inversion algorithm is applied to this limb radiance profile, the reference VER profile in Fig. 9 is exactly reproduced. Thus, the reference VER profile embodies the features of spherical symmetry that are inherently assumed in the 1-D Abel inversion, and Fig. 11 illustrates the implications of these assumptions on the VER limb path distributions for two representative tangent altitudes.

The rest of the VER retrievals in this section are designed to interrogate the influence of spatially localized emissions sources on the 1-D Abel inversion algorithm. To begin this investigation, the reference VER profile is modified by setting the FWHM(ψ) to 0.5 deg in the angular distribution associated with the vertical peak at 130 km. The angle of the maximum peak in the angular distribution is still set to zero (i.e., $\psi_p = 0$), however. As a result, the emission at 130 km is highly localized but still symmetric with respect to the radial distance at the tangent altitude. Fig. 12 shows the corresponding VER limb path distribution. Obviously, the VER limb path distribution is the same as in Fig. 11 for the 110 km tangent altitude, but the distribution at 130 km tangent altitude is spatially confined. The effective horizontal length of the emission source along the limb path can be computed using (42): $\Delta L = 2\Delta x = 2R_T(z)\tan(FWHM(\psi)/2)$, which gives $\Delta L \sim$ 60 km in this case. The simulated limb radiance for this VER distribution is shown in Fig. 10 and the retrieved

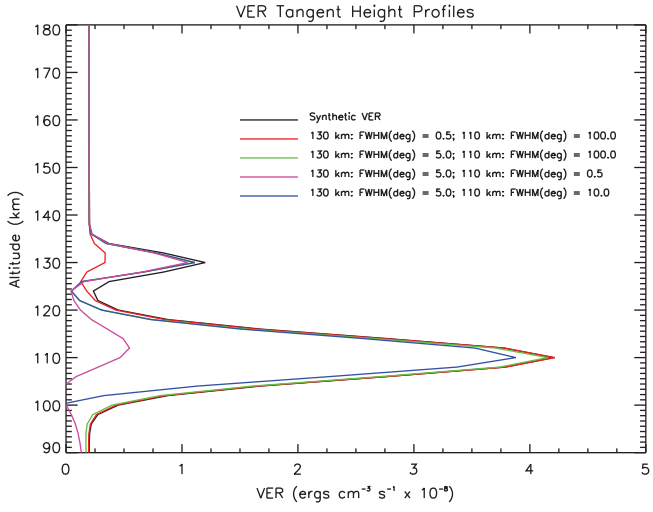

Fig. 9. The black solid line labeled 'Synthetic VER' is the reference VER profile described in Section 3. The other VER profiles were retrieved from simulated limb radiance using the 1-D Abel inversion algorithm. The simulated limb radiances (shown in the next figure) were computed from non-spherically symmetric emission sources. The parameterization of these emission sources is specified in the legend and described in the text.

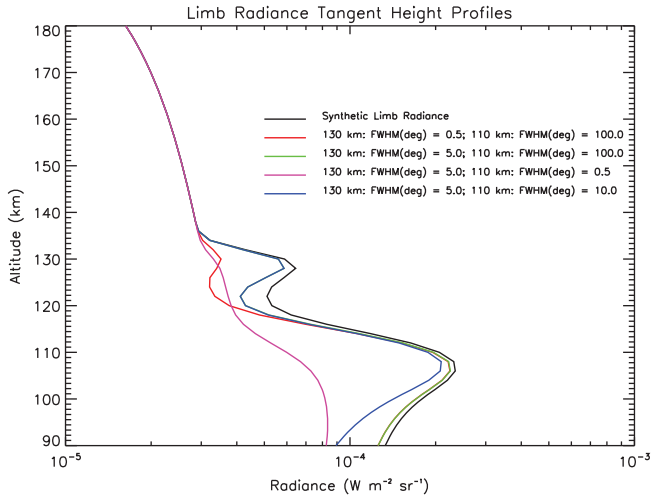

Fig. 10. Simulated limb radiance profiles from non-spherically symmetric VER distributions specified in the legend and described in Section 3. The previous figure shows the VER profiles retrieved from these limb radiances using the 1-D Abel inversion algorithm.

VER profile from the 1-D Abel inversion algorithm is shown in Fig. 9. Compared to the reference VER profile, the retrieved VER for this specified altitude–angular distribution reproduces the vertical structure near 110 km but barely shows an indication of a peak in VER at 130 km. If the FWHM(ψ) is smaller than 0.5 deg, then the retrieved VER profile from the 1-D Abel inversion algorithm shows no sign of a peak in the vertical structure at 130 km at all. Thus, an emission source at the tangent layer must have a horizontal length greater than 60 km along the limb path in order to begin to resolve the vertical features in the true VER profile from a 1-D Abel inversion of the limb radiance.

Continuing the above analysis, the next pertinent issue is the minimum horizontal length along the limb path required to resolve the vertical structure in the reference VER profile near the 130 km tangent altitude. Recall that this feature has a FWHM(z) of 5 km, which maps to a horizontal length of $\Delta x = 255$ km at 130 km tangent altitude. The FWHM(ψ) for this horizontal distance can be determined using (42) – i.e., FWHM(ψ) $= 2\tan^{-1}(x/R_T(z)) = 4.5$ deg. Modifying the reference VER profile such that FWHM(ψ) $= 5$ deg, with ψ_p still set to zero, produces a limb path VER distribution at 130 and 110 km tangent altitudes as shown in Fig. 13. The secondary peaks at the 110 km tangent height are significantly reduced compared to the secondary peaks corresponding to the reference VER profile shown in Fig. 9. The angles ψ of the secondary peaks at $x = \pm 510$ km along the 110 km tangent altitude are $\psi = \pm 4.5$ deg. Hence, the projection of vertical features near 130 km tangent altitude onto the 110 km tangent altitude limb path are attenuated by a factor of $\exp[-\psi^2/2\sigma_\psi^2] = \exp[-(4.5/2.123)^2/2] \sim 0.1$, where $\sigma_\psi = 2.355 \times$ FWHM(ψ) $= 2.123$. Given the background value of V_o, the secondary peaks along the 110 km tangent altitude limb path should be on the order of 0.3×10^{-8} ergs cm^{-3} s^{-1},

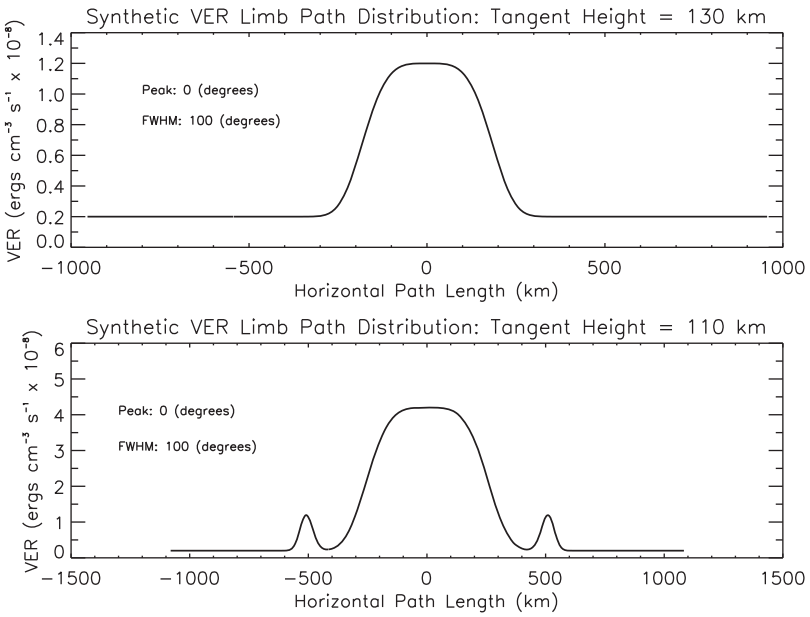

Fig. 11. Horizontal VER distribution along the limb-view path at 130 and 110 km tangent altitudes constructed from the reference VER profile shown in Fig. 9 and described in Section 3.

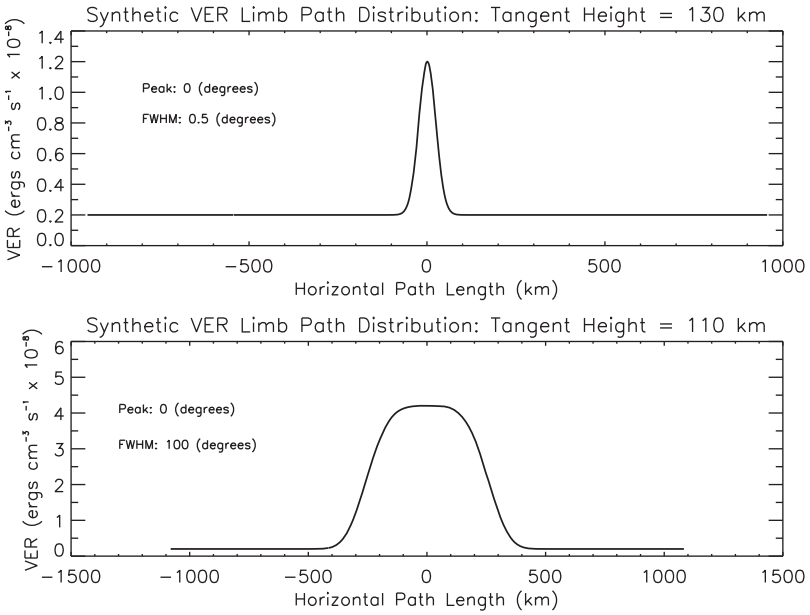

Fig. 12. Horizontal VER distribution along the limb-view path at 130 and 110 km tangent altitudes constructed from the non-spherically symmetric VER distribution specified in the legend and described in Section 3.

which is confirmed in Fig. 13. The limb radiance for this altitude–angular distribution is shown in Fig. 10 and the retrieved VER profile from the 1-D Abel inversion algorithm is shown in Fig. 9, indicating that the vertical features near 130 km are resolved. In conclusion, an emission source centered at 130 km tangent altitude requires a horizontal length greater than 255 km to resolve a 5 km vertical feature.

The next two retrieval studies retain the FWHM(ψ) = 5.0 deg in the angular distribution associated with the vertical peak at 130 km tangent altitude. The angular distribution associated with the vertical peak at 110 km is now set to a FWHM(ψ) of 0.5 and 10 deg. In all cases, the peak in the angular distributions is set to zero (i.e., $\psi_p = 0$). The VER limb path distributions are not shown for these two cases since its not difficult to imagine their form given the results shown in Figs. 12 and 13. The limb radiances for these two altitude–angular VER distributions are shown in Fig. 10 and the retrieved profiles from the 1-D Abel inversion algorithm are shown in Fig. 9. Similar to the case shown in

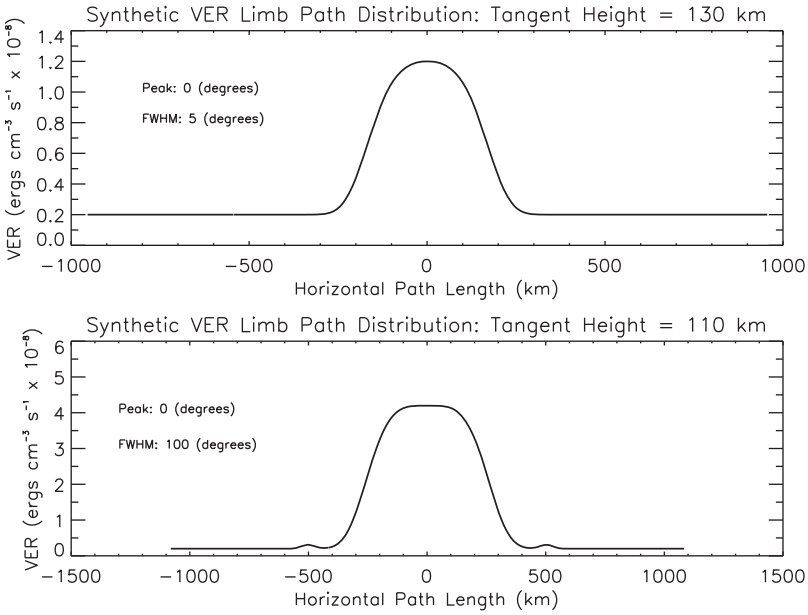

Fig. 13. Horizontal VER distribution along the limb-view path at 130 and 110 km tangent altitudes constructed from the non-spherically symmetric VER distribution specified in the legend and described in Section 3.

Fig. 12, a FWHM(ψ) of 0.5 deg for the angular distribution associated with the vertical peak at 110 km yields a retrieved VER profile that just begins to resolve the vertical features near 110 km tangent altitude. The FWHM(z) of 10 km maps to a horizontal length of $x = 360$ km at the 110 km tangent altitude. Using (42), the FWHM(ψ) for this horizontal distance is 6.4 deg. And if the FWHM(ψ) is set to 10 deg in the angular distribution associated with the vertical peak at 110 km, then the 1-D Abel inversion can resolve the 10 km vertical structure near the 110 km tangent altitude, as is evident from the VER retrieval result shown in Fig. 9.

The spatially localized emission sources examined so far have been symmetric with respect to the tangent altitude. The next study investigates the influence of localized emissions sources that do not spatially coincide with the tangent layer (i.e., non-tangent layer) on the 1-D Abel inversion algorithm. The parameter specification for the VER altitude–angular distributions was chosen such that vertical peaks at the 130 and 110 km tangent altitudes in the reference VER profile are barely discernable in the retrieved VER profile. The peaks in the angular distributions associated with both the 130 and 110 km tangent altitudes are defined as $\psi_p = 5$ deg. The FWHM(ψ) are also set to 5 deg in both angular distributions. This parameter specification defines a localized emission source that is displaced from the tangent altitude and positioned on the spacecraft side of the limb-view path. Since the emissions are optically thin, the results are independent of which side of the tangent layer that the emissions originate. Using (42), the emission source has a horizontal path length of $\Delta x = 570$ km centered at 566 km, based on the above parameter specification.

The limb path VER distributions for the localized, non-tangent layer emission source described in the above paragraph are shown in Fig. 14. For the 130 km tangent altitude, the horizontal distance of the localized emission source samples the high altitudes in the VER altitude distribution where g_z is effectively zero. Thus, the VER limb path distribution is constant at the background level V_o over the range $\Delta x = 570$ km centered at 566 km. Recall that the VER altitude distribution with the peak at 130 km begins to increase above the background level at 137 km, which corresponds to a horizontal distance of $x = 300$ km. Thus, Fig. 14 shows an increase in the VER limb path distribution above the background level for horizontal distances less than 300 km. The peak in the limb path VER distribution for $x < 300$ km occurs at the maximum in the product of g_z and g_ψ. At 130 km tangent altitude, the maximum in $g_z \times g_\psi$ occurs at $x = 140$ km, which corresponds to an altitude of 131.5 km and an angle of $\psi = 1.23$ deg. At this altitude–angular coordinate, $g_z = !\,0.78$ and $g_\psi = 0.21$. As a result, the peak VER in the limb path distribution should be 0.36 ergs cm^{-3} s^{-1}, which is verified by Fig. 14.

The limb path VER distribution at 110 km tangent altitude for the localized, non-tangent layer emission source described above is also shown in Fig. 14. Recall that the projection of the 130 km vertical peak onto the 110 km tangent altitude occurs at a horizontal distance of $x = 510$ km, which overlaps the localized emission source defined over the horizontal length of $\Delta x = 570$ km centered at 566 km. In fact, the projection of the 130 km vertical peak onto the 110 km tangent altitude is hardly attenuated at all since $g_\psi = 0.97$ at $x = 510$ km. The peak in the limb path VER distribution for $x < 510$ km is due to the vertical structure near 110 km. This peak corresponds with the maximum in the product of $g_z \times g_\psi$, as discussed above. For the 110 km tangent altitude, this maximum occurs at

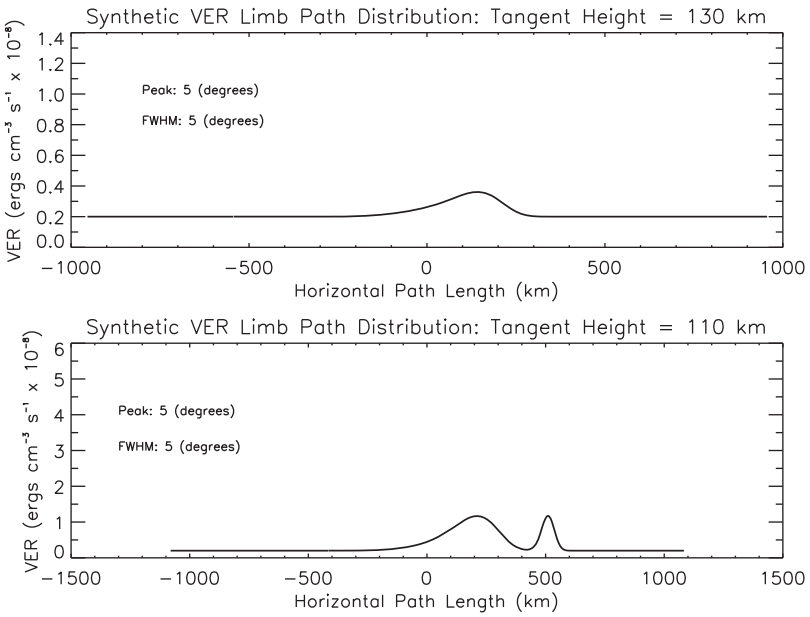

Fig. 14. Horizontal VER distribution along the limb-view path at 130 and 110 km tangent altitudes constructed from the non-spherically symmetric VER distribution specified in the legend and described in Section 3.

$x = 211$ km, corresponding to an altitude of 113 km and an angle of $\psi = 1.87$ deg. The distribution functions g_z and g_ψ are 0.72 and 0.24 at this altitude–angular coordinate, respectively. Consequently, the limb path VER distribution peak should be 1.18 ergs cm^{-3} s^{-1} at $x = 211$ km. This result is confirmed in Fig. 14.

Fig. 15 shows the 1-D Abel inversion VER retrieval for the localized, non-tangent layer emission source described above, which is compared to the reference VER profile. The vertical structure of the true VER profile is barely discernable in the VER retrieval from the localized, non-tangent layer emission source. Summarizing the above analysis of non-spherically symmetric emission sources, a few rules of thumb can be ascribed when retrieving VER profiles from a 1-D Abel inversion of limb radiance measurements in the 110–130 km altitude region. One, the threshold limb-view path horizontal distance for minimal detection is 60 km for tangent layer emission sources. Smaller scale auroral emission sources will not be detected at all. Two, an emission source must be within 250–500 km of the tangent location, and with a horizontal scale in the range 300–600 km along the limb-view path, as a minimal criterion for resolving the vertical structure of the emission rate. Three, to fully resolve the vertical structure of the emission rate, the emission source must overlap the tangent layer and have a horizontal scale along the limb-view path between $\Delta x = 250$ km and $\Delta x = 350$ km in order to resolve a 5 and 10 km vertical feature, respectively. Four, if the above criteria are not met, the retrieved VER profile will systematically underestimate the true VER profile.

4. Summary and conclusions

The STORM-E model is developed from $NO^+(v)$ VER derived from SABER 4.3 μm channel limb emission measurements. The STORM-E model will be integrated into the IRI source code, providing the first direct geomagnetic correction to the IRI E-region electron density peak concentration. In this paper, Part I of the series on the STORM-E model, the plausibility of using $NO^+(v)$ VER as a proxy for the E-region response to solar-geomagnetic activity is examined. Comparisons between precipitating auroral particle energy flux measured by NOAA/POES and SABER-derived outgoing ionosphere–thermosphere $NO^+(v)$ 4.3 μm radiative flux support the conjecture that $NO^+(v)$ VER is a prompt radiative response to auroral particle precipitation. The patterns of auroral particle energy flux and the outgoing $NO^+(v)$ 4.3 μm radiative flux share a similar morphology with correlation coefficients greater than 0.83 for the geomagnetic storms analyzed in this paper. Additional observational studies and theoretical modeling studies previously reported in the literature also indicate that $NO^+(v)$ 4.3 μm VER is a prompt indicator of the E-region response to particle precipitation in the auroral oval region (Mertens et al., 2007a,b, 2008, 2009a,b,c; Fernandez et al., 2010).

This paper presented a detailed description of the algorithms and methodologies used to derive $NO^+(v)$ VER from SABER 4.3 μm limb radiance measurements. There are two main steps: (1) remove the background contributions of $CO_2(v_3)$ emission from the measured 4.3 μm limb radiance using non-LTE radiation transfer models, and (2) perform an Abel inversion on the subsequent residual limb radiance to obtain vertical profiles of $NO^+(v)$ VER. An error analysis was conducted to quantify known sources of error in retrieving $NO^+(v)$ VER from SABER 4.3 μm channel limb emission measurements. The sources of uncertainty in the error analysis included radiometric calibration error, systematic modeling errors in removing

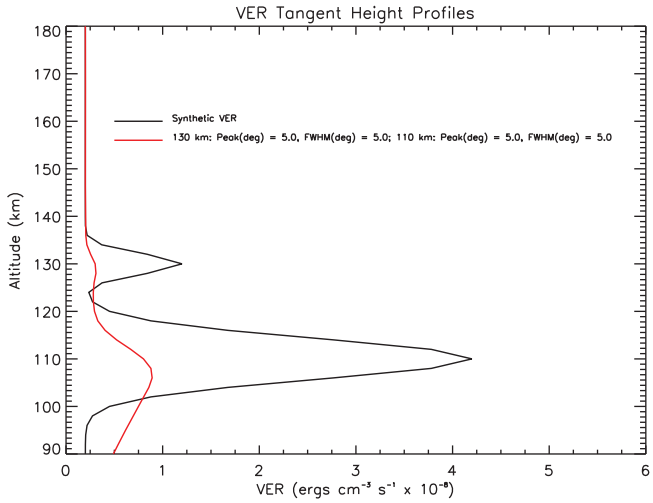

Fig. 15. The black solid line labeled 'Synthetic VER' is the reference VER profile described in Section 3. The other VER profile was retrieved from simulated limb radiance using the 1-D Abel inversion algorithm. The simulated limb radiance was computed from the non-spherically symmetric VER distribution specified in the legend and described in the text.

the background $CO_2(v_3)$ contribution from the measured SABER 4.3 μm channel limb radiance, and the influence of measurement noise on the retrieved $NO^+(v)$ VER profile. The influence of measurement noise on the Abel inversion algorithm induces both a systematic bias and a statistical uncertainty into the retrieved $NO^+(v)$ VER profile. The RMS error from these sources of uncertainty is 8%, considering the fact that the STORM-E model utilizes altitude-averaged $NO^+(v)$ VER data over the altitude range from 116 to 120 km (Mertens et al., submitted for publication).

Another source of uncertainty examined in this paper is the influence of spatially structured auroral $NO^+(v)$ emission sources on the 1-D Abel inversion algorithm. This source of uncertainty is difficult to quantify without foreknowledge of the spatial-temporal structure of the auroral $NO^+(v)$ emission during a particular SABER measurement event, or without independent observations coincident with SABER measurements. And these coincident measurements must be sufficient to obtain the true spatial structure of the auroral $NO^+(v)$ emission over the atmospheric volume sampled by the SABER measurement. Nevertheless, the retrieval simulations from 1-D Abel inversions of limb radiances from non-spherically symmetric emission sources enabled several of rules of thumb to be obtained. One, the threshold limb-view path horizontal distance for minimal detection is 60 km for tangent layer $NO^+(v)$ emission sources. Two, a $NO^+(v)$ emission source must be within 250–500 km of the tangent location, and with a horizontal scale in the range 300–600 km along the limb-view path, as a minimal criterion for resolving the vertical structure of the $NO^+(v)$ emission rate. Three, to fully resolve the vertical structure of the $NO^+(v)$ emission rate, the emission source must overlap the tangent layer and have a horizontal scale along the limb-view path between $\Delta x = 250$ km and $\Delta x = 350$ km in order to resolve a 5 and 10 km vertical feature, respectively.

If the spatial properties of the auroral $NO^+(v)$ emission sources do not satisfy the criteria described above, then the SABER-derived $NO^+(v)$ VER profile from the 1-D Abel inversion algorithm will systematically underestimate the true $NO^+(v)$ VER profile. Consequently, if there are enough SABER measurements of nighttime auroral 4.3 μm emission that violate the above criteria, then there may be a systematic underestimate in the STORM-E model predictions of geomagnetic enhancements in E-region peak electron densities. The only conclusive assessment of the effects of non-spherically symmetric auroral $NO^+(v)$ emission sources on STORM-E is to compare STORM-E predictions with independent measurements of E-region peak electron densities. In Part II of this series, the details of the empirical STORM-E model development are given (Mertens et al., submitted for publication). Furthermore, STORM-E model predictions are compared to incoherent scatter radar measurements of E-region electron densities for various geomagnetic storm periods during solar cycle 23.

References

Araujo-Pradere, E.A., Fuller-Rowell, T.J., Codrescu, M.V. STORM: an empirical storm-time ionospheric correction model 1. Model description. Radio Science 37 (5), 1070, http://dx.doi.org/10.1029/2001RS002467, 2002.

Araujo-Pradere, E.A., Fuller-Rowell, T.J., Bilitza, D. Validation of the STORM response in IRI2000. J. Geophys. Res. 108 (A3), 1120, http://dx.doi.org/10.1029/2002JA009720, 2003.

Araujo-Pradere, E.A., Fuller-Rowell, T.J. Time empirical ionospheric correction model (STORM) response in IRI2000 and challenges for empirical modeling in the future. Radio Science 39, RS1S24, http://dx.doi.org/10.1029/2002RS002805, 2004.

Arfken, G. Mathematical Methods for Physicists, third ed Academic Press, Orlando, 1985.

Bilitza, D., Reinisch, B.W. International Reference Ionosphere 2007: improvements and new parameters. Adv. Space Res. 42 (4), 599–609, http://dx.doi.org/10.1016/j.asr.2007.07.048, 2008.

Christensen, A.B., Paxton, L.J., Avery, S., et al. Initial observations with the Global Ultraviolet Imager (GUVI) in the NASA TIMED satellite mission. J. Geophys. Res. 108 (A12), 1451, http://dx.doi.org/10.1029/2003JA009918, 2003.

Fernandez, J.R., Mertens, C.J., Bilitza, D., Xu, X., Russell III, J.M., Mlynczak, M.G. Feasibility of developing an ionospheric E-region electron density storm model using the TIMED/SABER measurements. Adv. Space Res. 46, 1070–1077, 2010.

Fuller-Rowell, T.J., Araujo-Pradere, E., Codrescu, M.V. An empirical ionospheric storm-time correction model. Adv. Space Res. 25 (1), 139–146, 2000.

Goody, R.M., Yung, Y.L. Atmospheric Radiation. Oxford University Press, New York, 1989.

Gordley, L.L., Marshall, B.T., Chu, D.A. LINEPAK: algorithms for modeling spectral transmittance and radiance. J. Quant. Spectrosc. Radiat. Transfer 52 (5), 563–580, 1994.

Lopez-Puertas, R. Rodrigo, Molina, A., Taylor, F.W. A non-LTE radiative transfer model for infrared bands in the middle atmosphere. I. Theoretical basis and application to CO_2 15 m bands. J. Atmos. Terr. Phys. 48 (8), 729–748, 1986a.

Lopez-Puertas, R. Rodrigo, Lopez-Moreno, J.J., Taylor, F.W. A non-LTE radiative transfer model for infrared bands in the middle atmosphere. II. CO_2 (2.7 and 4.3 μm) and water vapor (6.3 μm) bands

and N2(1) and O2(1) vibrational levels. J. Atmos. Terr. Phys. 48 (8), 749–764, 1986b.

Lopez-Puertas, M., Zaragoza, G., Lopez-Valverde, M.A., Taylor, F.W. Non local thermodynamic equilibrium (LTE) atmospheric limb emission at 4.6 μm 1. An update of the CO_2 non-LTE radiative transfer model. J. Geophys. Res. 103 (D7), 8499–8513, 1998.

Lopez-Puertas, M., Garcia-Comas, M., Funke, B., Picard, R.H., Winick, J.R., Wintersteiner, P.P., Mlynczak, M.G., Mertens, C.J., Russell III, J.M., Gordley, L.L. Evidence for an OH(v) excitation mechanism of CO_2 4.3 μm nighttime emission from SABER/TIMED measurements. J. Geophys. Res. 109, D09307, http://dx.doi.org/10.1029/2003JD004383, 2004.

Marshall, B.T., Gordley, L.L., Chu, D.A. BANDPAK: algorithms for modeling broadband transmission and radiance. J. Quant. Spectrosc. Radiat. Transfer 52 (5), 581–599, 1994.

McDade, I.C., Llewellyn, E.J. Inversion techniques for recovering two-dimensional distributions of auroral emission rate from tomographic rocket photometer measurements. Can. J. Phys. 69, 1059–1068, 1991.

Mertens, C.J., Mlynczak, M.G., Lopez-Puertas, M., Wintersteiner, P.P., Picard, R.H., Winick, J.R., Gordley, L.L., Russell III, J.M. Retrieval of mesospheric and lower thermospheric kinetic temperature from measurements of CO_2 15 m Earth limb emission under non-LTE condition. Geophys. Res. Lett. 28 (7), 1391–1394, 2001.

Mertens, C.J., Mlynczak, M.G., Lopez-Puertas, M., Wintersteiner, P.P., Picard, R.H., Winick, J.R., Gordley, L.L., Russell III, J.M. Retrieval of kinetic temperature and carbon dioxide abundance from non-local thermodynamic equilibrium limb emission measurements made by the SABER instrument on the TIMED satellite, in: Proceedings of SPIE, Remote Sensing of Clouds and the Atmosphere VII, Agia Pelagia, Crete, Greece, September 24–27, vol. 4882, pp. 162–171, 2002.

Mertens, C.J., Schmidlin, F.J., Goldberg, R.A., Remsberg, E.E., Pesnell, W.D., Russell III, J.M., Mlynczak, M.G., Lopez-Puertas, M., Wintersteiner, P.P., Picard, R.H., Winick, J.R., Gordley, L.L. SABER observations of mesospheric temperatures and comparisons with falling sphere measurements taken during the 2002 summer MaCWAVE campaign. Geophys. Res. Lett. 31, L03105, http://dx.doi.org/10.1029/2003GL018605, 2004.

Mertens, C.J., Mast, J.C., Winick, J.R., Russell III, J.M., Mlynczak, M.G., Evans, D.S. Ionospheric E-region response to solar-geomagnetic storms observed by TIMED/SABER and application to IRI storm-model development. Adv. Space Res. 39, 715–728, 2007a.

Mertens, C.J., Winick, J.R., Russell III, J.M., Mlynczak, M.G., Evans, D.S., Bilitza, D., Xu, X. Empirical storm-time correction to the International Reference Ionosphere Model E-region electron density parameterizations using observations from TIMED/SABER, in: Proceedings of the SPIE, Remote Sensing of Clouds and the Atmosphere XII, Florence, Italy, September 17–19, vol. 6745, 2007b.

Mertens, C.J., Fernandez, J.R., Xu, X., Evans, D.S., Mlynczak, M.G., Russell III, J.M. A new source of auroral infrared emission observed by TIMED/SABER. Geophys. Res. Lett. 35, L17106, http://dx.doi.org/10.1029/2008GL034701, 2008.

Mertens, C.J., Winick, J.R., Picard, R.H., Evans, D.S., Lopez-Puertas, M., Wintersteiner, P.P., Xu, X., Mlynczak, M.G., Russell III, J.M. Influence of solar-geomagnetic disturbances on SABER measurements of 4.3 μm emission and the retrieval of kinetic temperature and carbon dioxide. Adv. Space Res. 43, 1325–1336, 2009a.

Mertens, C.J., Xu, X., Fernandez, J.R., Bilitza, D., Russell III, J.M., Mlynczak, M.G. Development of a geomagnetic storm correction to the International Reference Ionosphere E-region electron densities using TIMED/SABER observations, in: Proceedings of SPIE, Remote Sensing of Clouds and the Atmosphere XIV, Berlin, Germany, August 31–September 3, vol. 7475, 2009b.

Mertens, C.J., Russell III, J.M., Mlynczak, M.G., She, C.-Y., Schmidlin, F.J., Goldberg, R.A., Lopez-Purtas, M., Wintersteiner, P.P., Picard, R.H., Winick, J.R., Xu, X. Kinetic temperature and carbon dioxide from broadband infrared limb emission measurements taken from the TIMED/SABER instrument. Adv. Space Res. 43, 15–27, 2009c.

Mertens, C.J., Xu, X., Bilitza, D., Mlynczak, M.G., Russell III, J.M. Empirical STORM-E model: II. Geomagnetic corrections to ionospheric E-region electron densities. Adv. Space Res., submitted for publication.

Mlynczak, M.G., Zhou, D.K., Adler-Golden, S.M. Kinetic and spectroscopic requirements for the inference of chemical heating rates and atomic hydrogen densities from OH Meinel band measurements. Geophys. Res. Lett. 25 (5), 647–650, 1998.

Mlynczak, M.G., Martin-Torres, F.J., Crowley, G., Kratz, D.P., Funke, B., Lopez-Puertas, M., Russell III, J.M., Kozyra, J., Mertens, C., Sharma, R., Gordley, L., Picard, D., Winick, J., Paxton, L. Energy transport in the thermosphere during the solar storms of April 2002. J. Geophys. Res. 110, A12S25, http://dx.doi.org/10.1029/2005JA011142, 2002.

Nebel, H., Wintersteiner, P.P., Picard, R.H., Winick, J.R., Sharma, R.D. CO_2 non-local thermodynamic equilibrium radiative excitation and infrared dayglow at 4.3 μm: application to Spectral Infrared Rocket Experiment data. J. Geophys. Res. 99 (D5), 10,409–10,419, 1994.

Phillips, B.L. A technique for the numerical solution of certain integral equations of the first kind. J. ACM 9, 84–97, 1962.

Picone, J.M., Hedin, A.E., Drob, D.P., Aikin, A.C. NRLMSIS-00 empirical model of the atmosphere: statistical comparisons and scientific issues. J. Geophys. Res. 107 (A12), 1468, http://dx.doi.org/10.1029/2002JA009430, 2002.

Russell III, J.M., Mlynczak, M.G., Gordley, L.L., Tansock, J., Esplin, R. An overview of the SABER experiment and preliminary calibration results, in: Proceedings of the SPIE 44th Annual Meeting, Denver, Colorado, July 18–23, vol. 3756, pp. 277–288, 1999.

Sharma, R.D., Wintersteiner, P.P. CO_2 component of daytime earth limb emission at 2.7 micrometer. J. Geophys. Res. 90 (A10), 9789–9803, 1985.

Solomon, S.C., Hays, P.B., Abreu, V.J. Tomographic inversion of satellite photometry. Appl. Opt. 23 (19), 3409–3414, 1984.

Tikhonov, A.N. On the solution of incorrectly stated problems and the method of regularization. Dokl. Akad. Nauk SSSR 151, 501–504, 1963.

Twomey, S. On the numerical solution of Fredholm integral equations of the first kind by the inversion of the linear system produced by quadrature. J. Assoc. Comput. 10, 97–101, 1963.

Twomey, S. Introduction to the Mathematics of Inversion in Remote Sensing and Indirect Measurements. Elsevier, New York, 1977.

Winick, J.R., Picard, R.H., Sharma, R.D., Joseph, R.A., Wintersteiner, P.P. Radiative transfer effects on aurora enhanced 4.3 micron emission. Adv. Space Res. 7 (10), 17–21, 1987a.

Winick, J.R., Picard, R.H., Joseph, R.A., Sharma, R.D., Wintersteiner, P.P. An infrared spectral radiance code for the auroral thermosphere (AARC), Rep. AFGL-TR-87-0334. Air Force Geophysical Laboratory, Hanscom Air Force Base, Massachusetts, 1987b.

Wintersteiner, P.P., Picard, R.H., Sharma, R.D., Winick, J.R., Joseph, R.A. Line-by-line radiative excitation model for the non-equilibrium atmosphere: application to CO_2 15 μm emission. J. Geophys. Res. 97 (D16), 18,083–18,117, 1992.